16

Diagnostic Indicators for Shipboard Systems using Non-Intrusive Load Monitoring

by

Thomas W. DeNucci

B.S., Electrical Engineering, U.S. Coast Guard Academy, 1998

Submitted to the Department of Mechanical Engineering in Partial Fulfillment of the Requirements for the Degrees of

Master of Science in Naval Architecture and Marine Engineering
Master of Science in Mechanical Engineering

at the
Massachusetts Institute of Technology

June 2005

Signature of Author _____
Department of Ocean Engineering and the
Department of Mechanical Engineering
May 13, 2005

Certified by _____
Steven B. Leeb, Associate Professor of Electrical Engineering and Computer Science
Department of Electrical Engineering and Computer Science
Thesis Supervisor

Certified by _____
Timothy J. McCoy, Associate Professor of Naval Construction and Engineering
Department of Mechanical Engineering
Thesis Reader

Certified by _____
David L. Trumper, Professor of Mechanical Engineering
Department of Mechanical Engineering
Thesis Reader

Certified by _____
Robert W. Cox, Doctoral Candidate
Department of Electrical Engineering
Thesis Reader

Accepted by _____
Michael Triantafyllou, Professor of Ocean Engineering
Chairman, Department Committee on Graduate Students
Department of Ocean Engineering

Accepted by _____
Lallit Anand, Professor of Mechanical Engineering
Chairman, Department Committee on Graduate Students
Department of Mechanical Engineering

Page Intentionally Left Blank

Diagnostic Indicators for Shipboard Systems using Non-Intrusive Load Monitoring

by

Thomas W. DeNucci

Submitted to the Department of Ocean Engineering and the Department of Mechanical Engineering in Partial Fulfillment of the Requirements for the Degrees of

Master of Science in Naval Architecture and Marine Engineering

and

Master of Science in Mechanical Engineering

ABSTRACT

Field studies have demonstrated that the Non-Intrusive Load monitor (NILM) can provide real-time indication of the condition of electro-mechanical systems on board naval vessels. Results from data collected from engineering systems on board *USCGC SENECA (WMEC-906)*, a 270-foot U.S. Coast Guard cutter, indicate that the NILM can effectively identify faults, failures and deviations from normal operating conditions on numerous shipboard engineering systems.

Data collected from the sewage system identified metrics that can be applied, for example, to cycling systems (high pressure air, hydraulic systems, etc.) to differentiate between periods of heavy usage and fault conditions. Sewage system variability and randomness was minimized by employing a MATLAB simulation designed to permit exploration of system behavior that might not have been exposed during other conditions. Simulation data suggests that the presence, location and magnitude of a spike in the pump run distribution indicated the presence of a leak. Data from the actual shipboard system, when subjected to a quantifiable leak, displayed the same behavior.

Data collected from the Auxiliary Seawater (ASW) System indicated that the NILM is able to predict the failure of a flexible coupling linking the pump and motor components. The ASW motor-pump system was modeled using a 5^{th} order induction motor simulation to explore the electro-mechanical relationships between the motor, coupling and pump. Changes to the mechanical parameters of the coupling were captured in the electrical signature of the motor in both the simulation and shipboard data.

Frequency domain analysis of the ASW System data also suggested that the clogging of a heat exchanger on a critical shipboard system can be identified with the NILM, although the extent of diagnosis is dependent on the system flow patterns. Further development of hardware and software, along with continued research into the behavior of shipboard systems, will allow the NILM to augment existing monitoring systems and potentially serve as a stand-alone indicator of critical system performance.

Thesis Advisor: Steven B. Leeb
Title: Associate Professor of Electrical Engineering and Computer Science

Acknowledgements

The author would like to acknowledge the following organizations and individuals for their assistance. Without them this thesis would not have been possible.

- The Office of Naval Research's Control Challenge, ONR/ESRDC Electric Ship Integration Initiative and the Grainger Foundation, all of whom provided funding.
- LCDR Andy McGurer, LT Mike Obar, MKC Gadbois, MK1 Kiley and MK1 Labrier for their support on *CGC SENECA*.
- Jim Paris and Chris Laughman for the technical support rendered.
- Rob Cox, for the exceptional technical assistance and editorial comments.
- CDR Timothy J. McCoy and Professor David L. Trumper for advising me in the capacity of thesis readers.
- Finally, Professor Steven Leeb, thanks for being an outstanding thesis advisor and always keeping it real.

This thesis is dedicated to my wife, Amy E. DeNucci.

Table of Contents

List of Figures

List of Tables

Page Intentionally Left Blank

Chapter 1 Introduction

1.1 Motivation for Research

The Non-Intrusive Load Monitor (NILM) is a device that determines the operating schedule of all of the major loads on an electrical service using only measurements of the input voltage and aggregate current [1],[2]. The NILM has already been demonstrated effective in residential, commercial [3],[4] and automotive environments [5]. The research presented in this thesis applies the concept of non-intrusive load monitoring to shipboard engineering systems. Specifically, two shipboard diagnostic indicators are presented as stand-alone indicators of critical system performance. Other important engineering systems also examined in this thesis. The results demonstrate the potential of the NILM for monitoring electrical loads on naval vessels, providing back up indications of system performance, trending equipment performance and detecting different fault conditions.

1.2 Increased Electrical Demand in Today's Naval Vessels

In today's modern Navy, there is a growing trend of "electrification" that is causing major changes on both the generation and load sides of a vessel's electrical network. Figure 1-1 charts the trend of electric generating capacity of U.S. Navy Destroyers over the last century [6]. On the supply side, the Navy is currently exploring the use of integrated power systems to increase plant operating efficiency and the ability to reconfigure the electrical distribution system in a battle scenario. On the demand side, there has been a marked increase in the number, type and variety of electrical loads. Advances in computing and power electronics have made it possible to replace many mechanical, hydraulic, and pneumatic systems with more efficient and reliable electrical or hybrid electrical systems [6].

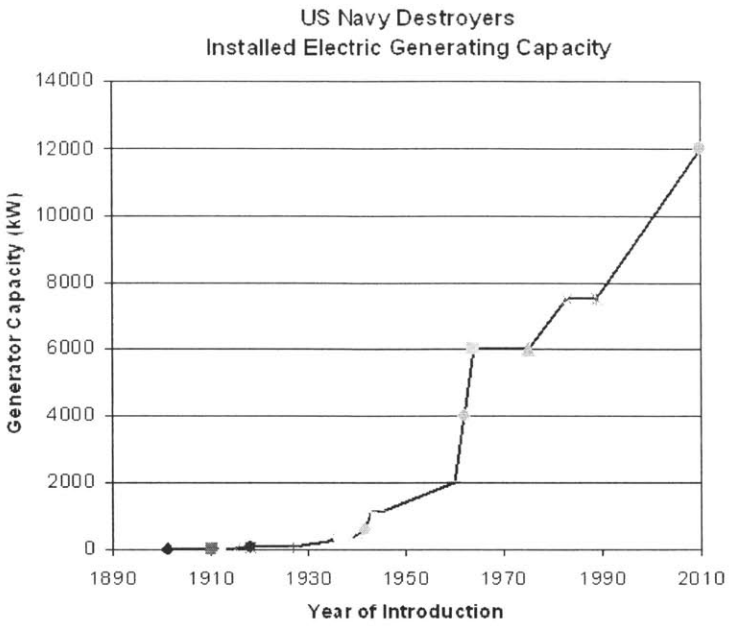

Figure 1-1: Electric Generating Capacity of US Navy Destroyers (1910-2010 projected)

As shown in Figure 1-1, the electrical demand of Navy destroyers is only expected to increase in future years. All of these changes create a pressure for monitoring tools that can reliably provide real-time information regarding the behavior of individual loads and the quality of the power delivered to them [7],[8].

1.3 The NILM as a Monitoring Tool

As shipboard engineering plants became more and more technologically sophisticated, the need for reliable plant monitoring became paramount. Today, engineering plants are often equipped with high quality data logging systems that collect measurements made by numerous transducers. They may also record information entered manually by the crew. For instance, the *USCGC SENECA (WMEC-906)* is equipped with a system that records changes in main engine revolutions on a per minute basis. Although these types of monitoring systems alleviate watchstander burden, they do not provide any analysis, control or casualty prevention functions.

As suggested above, traditional monitoring systems are beleaguered by two key limitations:

- Human interaction is required to collect and analyze the data;
- In order to obtain useful information, a complex and expensive sensor network is required.

While mass production has reduced the cost of many sensors, the cost of sensor installation and maintenance still remains high. In an effort to reduce costs, ships have employed a paradigm of "fewer sensors." Although this has resulted in both an initial and total life-cycle cost savings, the decrease in the number of sensors has caused an increase in the number of possible points of critical failure. This scope of this trade-off is particularly important in combat vessels, where the inadvertent failure of individual sensors could potentially hinder damage assessment, reconstruction, or fight-through efforts.

Two critical requirements of an ideal shipboard monitoring tool are that it should automate the analysis of sensor data and that it should minimize the need for a large array of sensors. The NILM performs both of these tasks. It makes "dual-use" of the power system, which continues to serve its primary function of delivering power to loads, but which also becomes an information network for monitoring the behavior of these loads based on power demand. The NILM requires only a set of voltage and aggregate current measurements made at a single or a limited number of points in the power system. It operates with a comparatively small sensor network. This benefit comes at the cost of requiring sophisticated signal processing to disaggregate information about individual loads. The NILM therefore offers a trade-off between hardware installation, data processing and collation complexity, and the risk of failing to identify an important pathological or diagnostic condition. At a minimum, the NILM offers a valuable opportunity to add redundancy inexpensively in an overall suite of shipboard monitoring tools. It is also conceivable that data from the NILM could serve as an automated data stream for current or anticipated monitoring systems like ICAS [8].

The hardware required for the NILM is relatively low-cost compared to a custom sensor network. The commercial-off-the-shelf (COTS) NILM computer can easily be programmed to analyze data automatically and to send the ship's engineering crew regular status reports. A typical NILM system today costs about $1,000, but with economies of scale a large number of NILM systems could be produced at a significantly lower cost.

1.4 Objective and Outline of Thesis

The research presented in this thesis is a continuation of the efforts conducted by LCDR Jack S. Ramsey, Jr., USN [9]. In his thesis, LCDR Ramsey tested the feasibility of the NILM concept in the shipboard environment by installing basic NILM hardware on three different ships. His results were promising and he concluded that the NILM could successfully complement the engineering system architecture in identifying faults and pathological conditions.

The purpose of this thesis was to develop specific diagnostic indicators for some of the shipboard engineering systems considered in [9]. Chapter 2 discusses NILM theory, application and power measurement techniques. Important features of the NILM system will also be restated in this chapter and specific hardware improvements and data analyzing processes will also be presented. Chapter 3 and Chapter 4 discuss diagnostic indicators for cycling systems and flexible coupled systems respectively. Chapter 5 presents further exploration of strainer clogging phenomenon originally presented in [9]. Chapter 6 discusses installation of a NILM on a reverse osmosis system while Chapter 7 presents recommendations, future work and conclusions.

Chapter 2 Background

2.1 NILM Background

The NILM uses voltage and current measurements to estimate real and reactive power consumption. Voltage and current measurements are collected using COTS transducers. The NILM analyzes the aggregate current signal with a Pentium class PC and signal processing and parameter estimation algorithms that can determine the operating state of individual loads [3], [10]. Specific information on NILM hardware, software and installation can be obtained in [9].

The NILM has a relatively high data capture rate suitable for monitoring and detecting transients. The ability to monitor short transients permits the NILM to accurately detect changes in electro-mechanical systems. Electro-mechanical devices must be considered as systems, that is, operation is effected by the electrical elements on one side of the system and mechanical parameters on the other. The relationship between the electrical and mechanical sides of the systems is typically apparent in the electrical transient of the system.

The NILM is also capable of tracking the operating schedule of significant electrical loads on a power distribution system [11]. It can also use measurements of the current flowing into the stator terminals of an induction motor to track and trend all of the key motor resistances, inductances, and mechanical shaft parameters [12],[13]. This can potentially preclude the need for complicated sensor arrays that measure motor flux in order to study motor behavior. The NILM can also be used to diagnose faults that commonly occur in electromechanical systems like HVAC plants [14]. The NILM's ability to examine harmonic current information can be used to create performance metrics for variable speed drives and to study the electrical interference caused by power converters [4].

2.2 NILM Power Measurement on Electrical Systems

In a single phase grounded system, power measurement with the NILM is relatively straight forward. The NILM is supplied with voltage from line to neutral and current from any load downstream of the monitoring point. Real power is calculated using current which is in-phase with voltage while reactive power is calculated from current components that are 90° out of phase with voltage. In a single phase system, real power is the first column of the data output file produced by the NILM software, while reactive power is the second.

In a three phase ungrounded electrical system, such as those on naval vessels, power measurement is more complex. The voltage observed by the NILM is typically line-to-line (there is no ground). Due to the three voltage-current pairs and their phase relationships in a three phase system, care must be taken to associate three phase measurements with equivalent measurements on a single phase system [9]. Useful relationships between line-to-line voltages and currents in three phase and single phase systems are exploited in many commercially available power measurement products such as the FlukeMeter. Generally speaking, when measuring three phase systems in applications for this thesis, voltage is measured across two of the phases and current is measured through the third. For a better understanding of how the NILM determines real and reactive power see [15].

The NILM output is formatted as an eight column matrix that contains values for the real power, the reactive power and their associated harmonics. The matrix column corresponding to each of these power quantities depends on the number of electrical phases in the system being measured. In a single phase system, the values for the real power are contained in the 1st column of the matrix while the values for the reactive power are contained in the 2nd column. In the case of three phase power, these relationships are reversed; the values for reactive power are contained in the 1st column of the matrix while the values for the "negative" real power are contained in the 1st column. Table 2-1 explains the relationships for the single and three phase power system.

Table 2-1: Real and Reactive Power Measurement

	Column of Data File	
	Real Power	**Reactive Power**
Single Phase System	1st	2nd
Three Phase System	-2nd	1st

2.3 NILM Test Bed

The importance of collecting actual real-time shipboard data cannot be understated. Although the lab can be a good environment for data collection and replication, the complexity and realistic element of shipboard data is preferred. The NILM data used in this thesis was collected almost exclusively on the *USCGC SENECA (WMEC-906)* home-ported in Boston, Massachusetts. The *SENECA* is one of thirteen Famous Class Medium Endurance Cutters in the U.S. Coast Guard fleet. These cutters have a length of 270' and a displacement of 1,825 tons. The Famous Class cutter is shown below in figure 2-2.

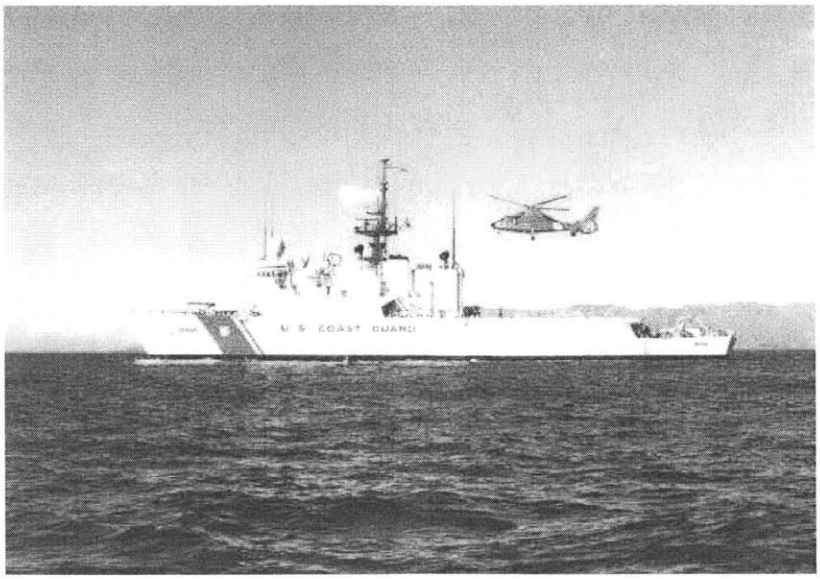

Figure 2-1: USCG Famous Class Medium endurance Cutter

The *SENECA* was an outstanding test bed because of its geographic location, accessibility and the willingness of the crew to assist in the data collection. There are 7 NILM systems currently installed on the cutter. Tables 2-2 and 2-3 list the location of each NILM system and its associated hardware specifications.

Table 2-2: NILM Systems on *USCGC SENECA*

Shipboard Engineering System	Compartment	NILM Computer Permanently Installed?
Auxiliary Seawater System	Auxiliary 2 (3-82-0-E)	Y
Roll-Fin Stabilizer System	Auxiliary 2 (3-28-0-E)	N
Laundry Transformer	Laundry Room (1-47-1-Q)	Y
Reverse Osmosis System	Auxiliary 1 (2-82-0-E)	Y
Sewage System	Auxiliary 1 (2-28-0-E)	Y
Steering System	Steering Gear Room (3-228-0-E)	N
Anchor Windlass	Anchor Windlass Room (1-12-0-Q)	N

Table 2-3: NILM Hardware Configuration on *SENECA*

System	Voltage Resistor (Ω)	Current Resistor (Ω)	Ref Resistor (Ω)	SF (KW/count)
ASW	130	7.5	56.2	0.0071
Fins	130	7.5	56.2	0.0057
Laundry	130	66.5	56.2	0.3841
Osmosis	130	66.5	56.2	To Be Determined
Sewage	130	66.5	56.2	0.000619
Steering	130	15	56.2	0.0063
Anchor Windlass	130	66.5	56.2	To Be Determined

2.4 Improvements to the NILM System

Numerous improvements to NILM hardware and data processing techniques were developed in the course of the past year. These changes primarily enhanced user interface with the NILM system and enabled collected data to be manipulated more easily.

2.4.1 Methodology for Accessing Collected Data

In this thesis, the NILM hardware was used as a data logger to collect windows of data for off-line analysis. The NILM hardware was configured to collect data in one-hour "snapshots". The ability to collect data manually, in smaller, discrete segments, is also available. In either case, the NILM hardware attaches a time/date stamp to the beginning and end of each data file. The time/date stamp appears in the following general format:

```
# nilm5 reopened = 20041214-070002
```

This format includes the snapshot date in the year/month/day format and the hour of the snapshot in twenty-four hour time. Although this method conveniently marks each file with time/date information, it creates a problem when analyzing the data with MATLAB or Octave. Unfortunately, these programs do not recognize the "#" prefix of the time/date stamp and thereby generate an error. In order to properly view the data, the time/date stamp must be stripped from the file using a text editor. Unfortunately, this is a very time consuming process because each file is compressed and is also extremely large (45 MB). For a single hour of data this process is tolerable, but for days or weeks of data this methodology is tedious and time consuming.

In an effort to increase efficiency and save time, a LINUX type environment for Windows, CYGWIN, was employed. This operating environment, coupled with author created PERL scripts, greatly reduced the overall time required to prepare data files for viewing and plotting. The PERL command to unzip the compressed data files, strip the time/date stamp from each file and save them as a text file is:

```
for i in *.gz; do echo $i; gunzip –c $i > tempfile; grep –v ^# tempfile > ${i/.gz/.txt};done
```

2.4.2 Hardware Improvements

Data transfer from the permanently installed NILM computers on the ship to removable media such as CD-R's also became very time consuming and tedious. It takes approximately 20 minutes to write about 18 hours worth of NILM data to a CD-R (about 3 hours to transfer 1 week of data). Aside from the overall time constraints, the necessity to change CD's every 20 minutes also became an inconvenience. To overcome this obstacle, DVD-RW drives were installed on the NILM computers. The DVD's are able to hold over five times the amount of data and took just over 20 minutes to write.

2.4.3 Ground Reference in Older NILM Systems

Some of the older NILM systems were improperly grounded to the computer SCSI Data Acquisition card. Although this does not seem to have affected the quality or resolution of the data in a three phase ungrounded system, care should be taken to ensure the ground reference pin on the SCSI interface is Pin 27, not Pin 26. All older NILM systems have been checked for this error and corrected, if necessary.

Chapter 3 Cycling System Diagnostics

3.1 Introduction

Cycling systems require periodic mechanical "charging" by an electromagnetic actuator like a pump or compressor. Examples include high-pressure air compressors, some pneumatic actuators, and vacuum-assisted drains and disposals. A casual inspection of such a system may fail to differentiate between periods of high usage and periods during which there exist pathological conditions such as leaks. This chapter presents how a NILM can be used to reliably distinguish between periods of heavy usage and leak conditions. In order to develop a metric that can reliably diagnose leak conditions in cycling systems, field experiments were conducted on *SENECA's* sewage system, which consists of vacuum-assisted drains and toilets. Using both experimental data and a simulation developed on the basis of this data, a reliable diagnostic indicator was developed. This chapter details the process and methods used to study the operation of the sewage system. Additionally, this chapter concludes with a brief discussion of several issues relevant to the design of an appropriate diagnostic indicator.

3.2 *SENECA* Sewage System

In order to discuss the details of the trend analysis performed using data collected from the Seneca's sewage system, it is necessary to describe the system's layout and typical operating behavior. In particular, all of *SENECA's* toilets, urinals and drains discharge into a vacuum collection tank. Vacuum is maintained in the tank by the operation of two alternately cycling pumps. When the system vacuum reaches a low vacuum set point (14 in. Hg), one of the two sewage vacuum pumps energizes to restore system vacuum. The on-line pump will secure when the high vacuum set point (18 in. Hg) is achieved. If for some reason the system vacuum is allowed to reach the low-low set point (12 in. Hg), then both pumps will energize and run until the high vacuum set point is restored. Figure 3-1 shows a picture of the *SENECA's* vacuum collection tank with the vacuum pumps in the foreground.

Figure 3-1: *USCGC SENECA* sewage system

To study the statistical behavior of the vacuum pump cycling, the NILM was configured to collect continuous "snapshots" of the real power delivered to the pumps. Figure 3-2 shows a typical data set consisting of the real power drawn by the pumps over a one hour period. Note that the data plotted in this Figure indicates sixteen distinct periods of pump operation. Each of the large amplitude, short duration spikes on the graph are a result of in-rush current generated by the pumps motors. Figure 3-3 presents this in more detail, showing the power drawn during the start-up, operation, and shut-down of one of the vacuum pumps.

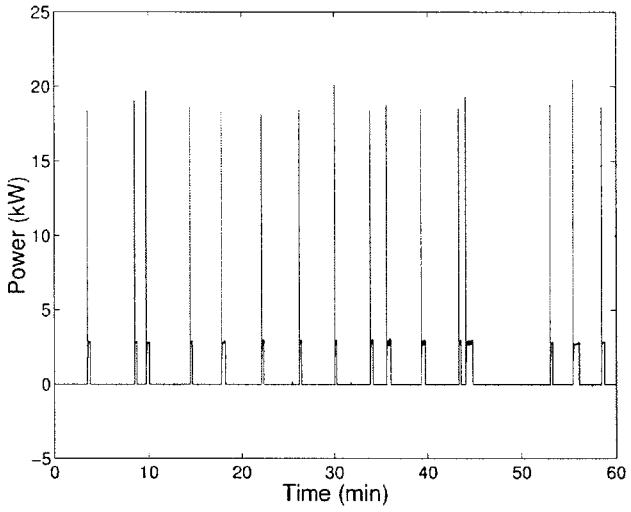

Figure 3-2: Vacuum Pump Transients

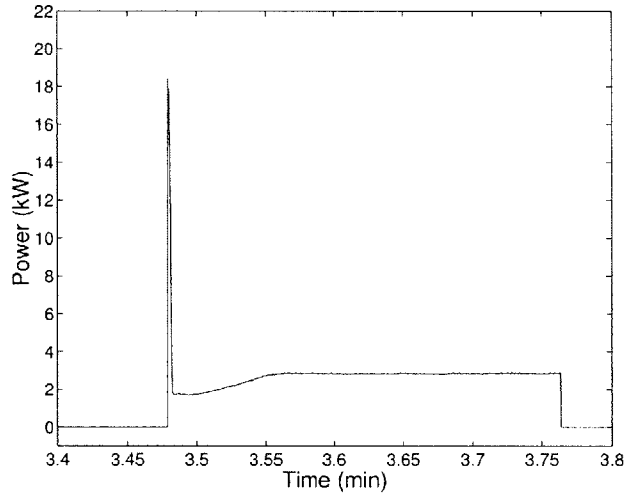

Figure 3-3: Vacuum Pump Real Power

3.3 Trend Analysis

Initially, it was unclear how it would be possible to differentiate between leaks and periods of high system usage. To begin, we examined NILM sewage data from *SENECA's* Fall 2003 patrol. Initially, we decided to examine the time between pump runs to see if it could provide any information related to system performance. In this particular instance, the time between pump runs is defined as the time that elapses from a pump shutdown to a subsequent pump start.

To begin the study of the sewage system data, software was developed to determine the underlying distribution of the time between pump runs. To perform this task, the software was designed to first calculate the time between each pump shutdown and the subsequent pump start. Using this information, the software outputs a histogram showing the distribution of the time between pump runs. A representative plot, which was formed using data from a four-week snapshot from October 24, 2003 to November 22, 2003), is shown in Figure 3-4.

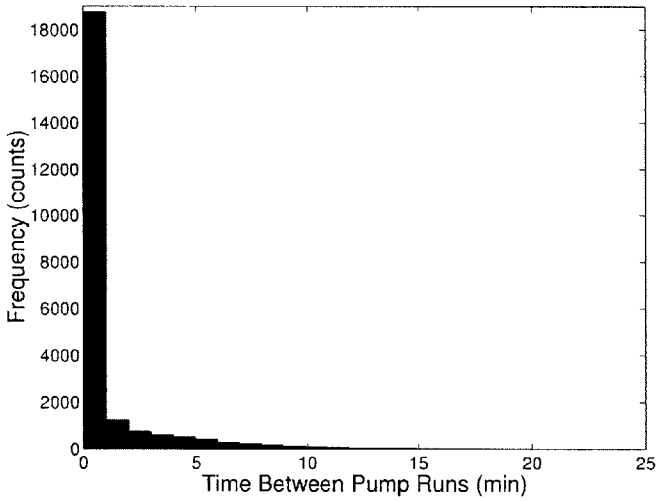

Figure 3-4: *SENECA* Cruise Profile (Time Between Pump Runs)

That data shown in Figure 3-4 underscores the inherent difficulty in determining a metric that can reliably discriminate between periods of high usage and periods during which leaks exist. In particular, the high frequency (>18,000) and short duration (< 1 min) of pump runs displayed in Figure 3-4 is not what was expected based on conversations with the crew [16]. According to their accounts, the average time between pump runs on an underway weekday should be approximately 6 minutes (10 pump runs per hour). Although the data presented in Figure 3-4 is inconsistent with the crew's assessment of past system behavior, it does not indicate whether the system was malfunctioning, or if the crew's usage was simply much higher than normal. Unfortunately, the shear magnitude of pump runs (indicated by a short time between pump runs) overwhelms and obscures the data that corresponds to a longer duration between pump runs.

Given the above findings, it was clear that further study was needed. Using an algorithm that detects statistical changes in the time between pump runs, it was discovered that there was a sharp increase in the time between pump runs on November 8th. Because the NILM captures data in one hour snapshots, it was even possible to note the hour of this change (1200). Based on this observation, the data was split into two parts to be analyzed separately, hoping that this might unmask any trends hidden by the shear number of runs. Histograms of the time between pump runs for each of the two week periods before and after 1200 on November 8th are shown in Figures 3-5 and 3-6, respectively.

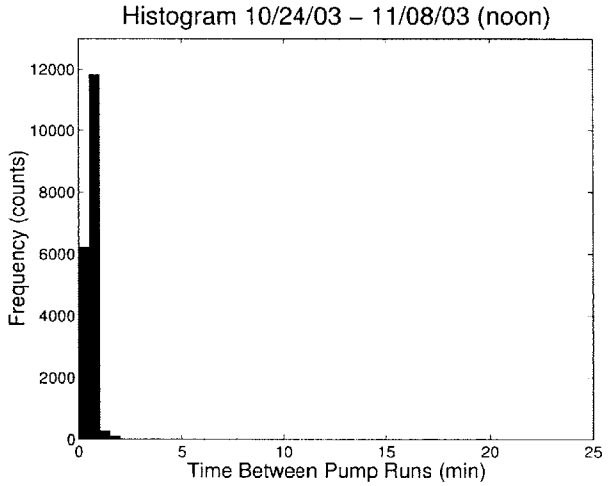

Figure 3-5: *SENECA* Cruise Profile (10/24-11/8)

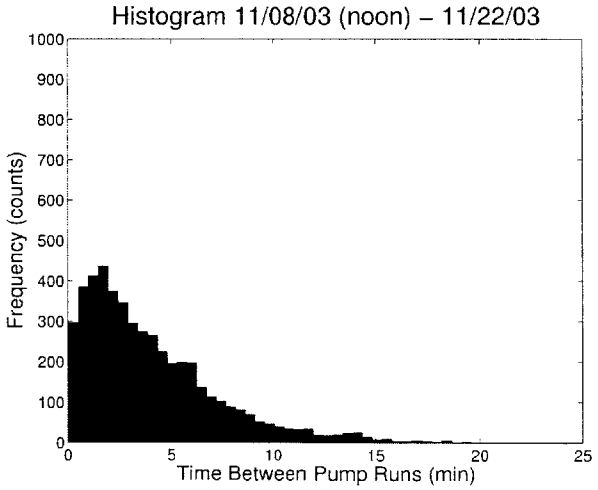

Figure 3-6: *SENECA* Cruise Profile (11/8-11/22)

The data in Figure 3-5 indicates that before noon on November 8th, the average time between pump runs was less than one minute; after noon on November 8th, as shown in Figure 3-6, that number significantly increased. From this data, it was proposed that some change in sewage system operation occurred on or about November 8th. After checking with the Engineer Officer of *SENECA* [16], he relayed that new check valves for the sewage system were ordered on November 6th and installed on either the 7th or the 8th. Given this information, it seems likely that the faulty check valves created the observed variation in the pump runs.

The initial study described in this section demonstrated that tracking the time between pump runs might provide and interesting indicator of sewage system health. Based on the observations presented here, it was decided to study this metric further by performing several experiments in order to determine the typical distribution of the time between pump runs and to determine the effect of introducing small, fixed leaks.

3.4 Crew Flushing Patterns

To determine how the time between pump runs is distributed, the flushing patterns of *SENECA's* crew were modeled. The magnitude of sewage system use varies according to the ship's schedule, the day of week and the time of the day. Assuming a no leak condition, sewage system activity is a function of the number of times that the sewage pumps run to restore system vacuum (i.e. a certain number of flushes will cause the sewage pumps to run). In order to identify trends in the flushing behavior of the crew, *SENECA* sewage system data was categorized into standard shipboard watch sections. Further, since the operational schedule of *SENECA* depends heavily on whether it is out at sea or in port, it was also decided to divide the data along these lines as well. Data was collected over six week inport period and an eight week underway period. The average number of pump runs per hour, per watch for various ship schedules and days of the week is presented in Table 3-1.

Table 3-1: Pump Run Patterns on *SENECA*

Watch Section	Average # of Pump Runs Inport (6 Weeks)		Average # Pump Runs Underway (8 Weeks)	
	Weekday	Weekend	Weekday	Weekend
0000-0400	5.75	5.5	10.5	22.25
0400-0800	13.5	6.5	10.5	21.75
0800-1200	13.75	10.5	13.25	28.5
1200-1600	16	9	12	30
1600-2000	10.75	14.5	13.75	27.5
2000-2400	8.75	10.25	12.5	23.5

3.4.1.1 Inport Flushing Patterns

Table 3-1 indicates several aspects of crew usage while the ship is inport. First, increased flushing activity is observed at meal time and at 0800, the time when watch sections relieve. On the weekend, there is a surge in system usage during the 0800-1200 watch; this is most likely due to watch section relief which occurs at 0900 on the weekends. Second, the system is used least during the late night and early morning hours when there are the fewest number of people on board the ship and when most are asleep. The 2000-2400 watch and the 0000-0400 watch experience relatively the same amount of system use regardless of the day of the week. Generally speaking, system use is higher during weekday working hours than during the same hours during the weekend. This is most likely caused by additional non-crew personnel aboard the ship during these times (civilian contractors, maintenance and support teams, guests and visitors).

3.4.1.2 Underway Flushing Patterns

As expected, the data presented in Table 3-1 indicates that crew usage is significantly different when SENECA is out on patrol. Underway, there is much more flushing activity on the weekend than there is during the week. This is most likely due to the increased free time and

absence of a regimented workday routine on the weekends. Again, increased flushing activity is observed around meal times. Another interesting observation in this data is that flushing activity on weekdays (inport and underway) follow similar usage patterns and are nearly the same order of magnitude while there is a marked difference between the inport and underway weekend data.

3.4.1.3 Flushing Probability Density Function

Although the number and frequency of sewage pump runs varies with the ship's schedule, the time of day, and the day of the week, the overall shape of the distribution for the time between pump runs remains fairly similar from watch to watch. Figure 3-7 shows histograms of the time between pump runs for each watch section while the ship was underway.

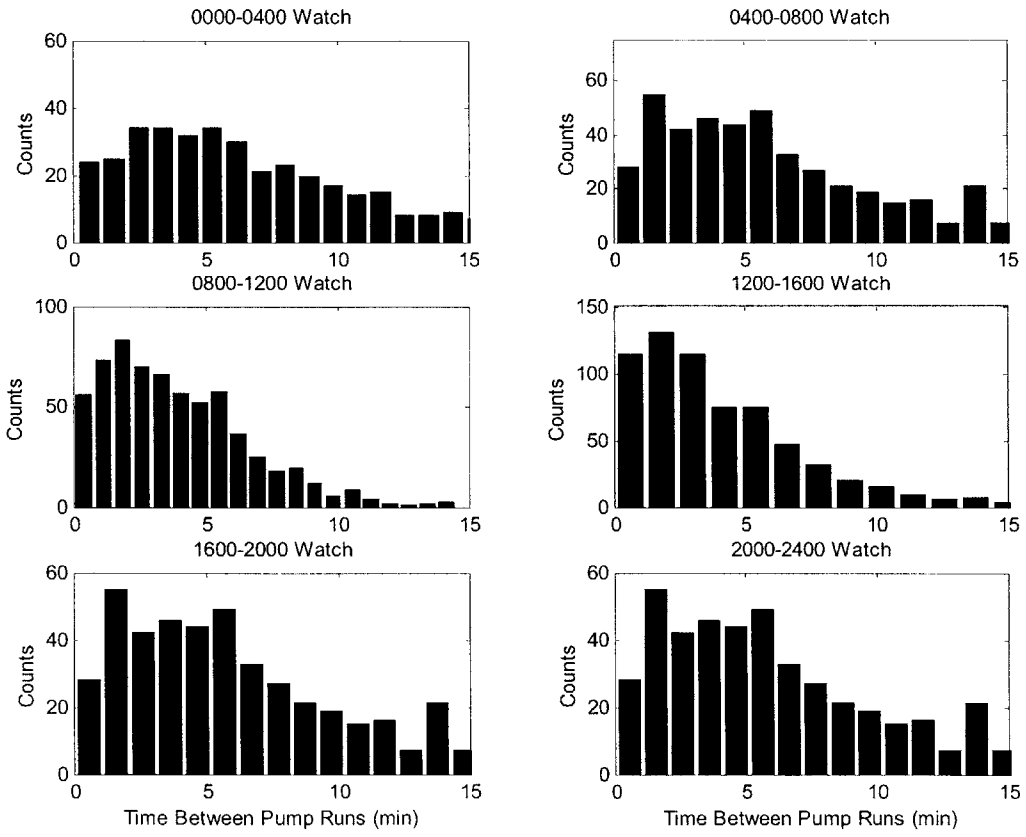

Figure 3-7: Flushing Distribution by Watches for Underway Data

Each of the histograms in Figure 3-7 indicates that the time between pump runs appears to approximate a Poisson process with exponentially distributed inter-arrival times. The basis for this claim is discussed further in the following section.

3.5 Describing the Crew Using the Poisson Process

As mentioned previously, the flushing behavior of *SENECA's* crew appears to be governed by a Poisson process, which is one of several stochastic processes that are commonly observed in nature. In particular, systems that involve the sequential arrival of numerous events are often best modeled as Poisson process in which individual events arrive according to an exponential distribution [17],[18]. For example, the arrival of data packets in networks often follows this type of behavior.

When a process is said to be Poisson, the time between the arrival of the $(k-1)^{th}$ event and the k^{th} event, which is denoted by using random variable T_k, is distributed according to the following probability density function (PDF):

$$f_{T_k} = \lambda e^{-\lambda t}$$

Eqn. 3-1

It should also be noted that T_k is also referred to as the inter-arrival time. From probability theory [18], it is known that the probability that T_k is less than or equal to some time t, is given by the cumulative density function (CDF):

$$P(T_k \leq t) = F_{T_k}(t) = \int_0^t \lambda e^{-\lambda \tau} d\tau = 1 - e^{-\lambda t}$$

Eqn. 3-2

Both the CDF and PDF for an exponentially distributed random variable where lambda is equal to 0.66[1] are plotted below in Figure 3-8.

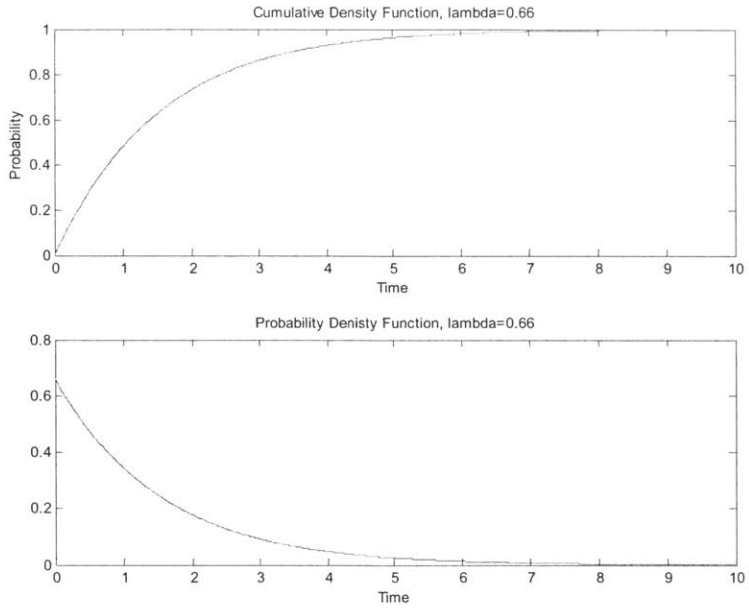

Figure 3-8: Cumulative Density Function and Probability Density Function

Given Eqn. 3-2, we choose R uniformly from [0,1] and return our inter-arrival time as T_k.

$$T_k = F_{T_k}^{-1}(R)$$

Eqn. 3-3

When events arrive according to a Poisson process, the real quantity of interest is often the time elapsed between the start of the process and the n^{th} arrival. From standard probability theory it can be shown that this time, which is denoted by the random variable Y_n, is given by the sum of the times between each of the subsequent arrivals [18]. Thus, Y_n is given by the equation:

[1] The reason we chose lambda equal to 0.66 will become apparent in later sections.

$$Y_n = T_1 + T_2 + \ldots + T_n$$

Eqn. 3-4

Since Y_n is the sum of several independent random variables, its distribution is given by the convolution of each of the individual PDF's [18]:

$$f_{Y_n}(y) = f_{T_1}(t) * f_{T_2}(t) * \ldots * f_{Tn}(t)$$

Eqn. 3-5

In this case, each T_k (i.e. inter-arrival time) is exponentially distributed with common parameter λ, and it can be shown that Y_n is thus distributed according to the Erlang PDF of order n [18] :

$$f_{Y_n}(y) = \frac{\lambda^n y^{(n-1)} e^{-\lambda y}}{(n-1)!}$$

Eqn. 3-6

Figure 3-9 shows a plot of the Erlang PDF of order 4 under the assumption that each arrival is exponentially distributed with lambda equal to 0.66. It is from this Figure that the motivation for the use of the Poisson process as a model for the crew's behavior becomes apparent. Compare Figure 3-9 with Figure 3-6 and each of the histograms shown in Figure 3-7. Clearly, the data plotted in each of these Figures follows the same overall trend. This is reasonable if one considers how the crew's behavior would influence the time between pump runs in the event that crew flushing is indeed a Poisson process. To see this, consider the simple case in which the sewage system does not have any leaks and in which each individual flush instantaneously removes the same amount of vacuum from the system. In that case there must be a fixed number of flushes that occur before the pump will operate. Assuming that N_{max} flushes are required and that the time between each flush is exponentially distributed with the common parameter λ, then the time between pump runs is a random variable which is the sum of the times between each flush. Thus, the time between pump runs should be distributed according to the

Erlang PDF of order N_{max}. This statement is entirely consistent with the data plotted in Figures 3-6, 3-7, and 3-9.

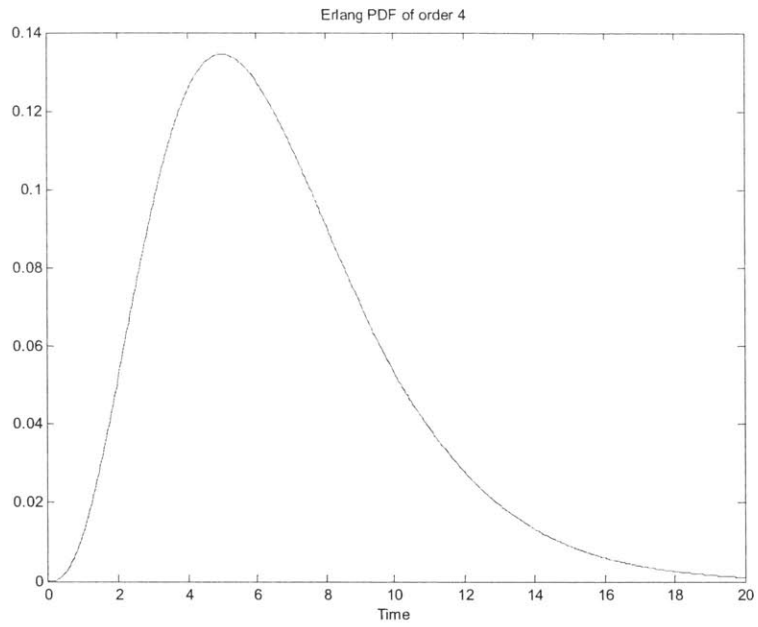

Figure 3-9: Erlang PDF of order 4

Given both the argument presented above and the fact that numerous arrival processes similar to this one can be modeled as Poisson [18], it was decided to use the Poisson model to describe the crew's flushing behavior. It is important to note, however, that while the Poisson model appears to be wholly reasonable in this case, it is necessary to conduct more extensive studies for longer periods of time and on several vessels before this statement can be made with extreme mathematical rigor. Although such exhaustive experimentation is planned for the future, the use of a Poisson model seems reasonable, especially given that the present task is to develop a diagnostic indicator.

3.6 MATLAB Sewage System Simulation

Cycling systems like the sewage system are influenced not only by physical conditions in the system but also by human behavior. For condition-based monitoring to succeed with a

minimum of false alarms, the NILM must be capable of distinguishing a genuine leak from increased system usage.

A problem with performing controlled tests on a cycling system is the inability to control the human element. It is possible to insert vacuum leaks of various sizes into the sewage system and to trend the resulting system cycles. It is more difficult to control usage by the ship's crew. Because of this, a statistical model for the sewage system using a MATLAB simulation was developed for use in devising a leak indicator or metric for the *SENECA*. For purposes of validation, the results of this simulation were compared to measured data.

It is important to remember that the purpose of developing the simulation was not to fit a statistical model to data, but to permit a thorough exploration of the system in the presence of a controlled crew model. Thus, we simulated the crew's behavior on the basis of the observations discussed in the previous section, which suggests that the crew's flushing patterns can be described as a Poisson process. The underlying assumptions imposed on this simulation are the following:

- Flushes occur with an exponentially distributed arrival times
- Every flush instantaneously removes the same amount of vacuum from the sewage system.
- Leak rate is constant regardless of system pressure (vacuum)

For purposes of the simulation, the time between flushes is calculated using the operating parameters of the sewage system as well as parameters consistent with the observed statistical distribution of the time between pump runs.

3.6.1 Generating Non-Uniform Random Variables

In order to emulate the operation of the sewage system, the simulator software must select a different random number to use for the time between each pair of subsequent flushes. To do so, it must generate a random number using an exponential distribution. When generating a set of random numbers that follow a non-uniform distribution, it is common to select a random value

from a uniform distribution and to convert this value to a random number that obeys the desired distribution. Two general techniques for performing this operation are the following:

- The inverse transform method
- The acceptance-rejection method

In the simulator, the inverse transform method is used to generate the inter-arrival times of the flushes. This method, which is described in detail below, relies on the fact that if y is a random variable on the interval [0,1], then the random variable $F^{-1}(y)$ will have its density equal to f(x).

To understand the inverse transform procedure used here to generate non-uniform random variables, first consider the relationship between a general random variable, X, and its corresponding CDF, $F_X(x)$. It is known from conventional theory that the probability that X is less than some given value x is equal to the value of the CDF evaluated at x. Stated mathematically, this says that:

$$P(X \leq x) = F_X(x)$$

Thus, the CDF for any random variable must have as its range the interval [0,1], regardless of how the random variable itself is distributed.

In order to generate random values using non-uniform distributions, we make use of the relationship between a random variable and its CDF. First, we randomly choose a value on the interval [0,1], and, thus, by definition this number must lie in the range of the given CDF. Next, we set the given CDF equal to the chosen random value and solve to find the corresponding input to the CDF. The result is thus a random number chosen from the desired non-uniform distribution.

In the simulator, each of the inter-arrival times is exponentially distributed, so to choose these times, we follow the above procedure. Thus, MATLAB's function rand is first used to choose a random variable R from the closed interval from 0 to 1. Then, the number R is set equal to the CDF of the general exponential random variable. Mathematically, this implies that:

$$F_T(t) = 1 - e^{-\lambda t} = R$$

Eqn. 3-7

Finally, Eqn. 3-6 is solved to generate an inter-arrival time. The simulated inter-arrival time, T_s, is given by the relation:

$$F_T^{-1}(R) = T_S = \frac{-\ln(1-R)}{\lambda}$$

Eqn. 3-8

The method used in the simulator to generate exponentially distributed inter-arrival times is the inverse transform methods mentioned above. In order to show this method is acceptable in this application, we must prove that T_s (simulated flush time) has the same distribution as T_k. To do this we must essentially prove that:

$$P(T_s \leq t) = P(T_k \leq t)$$

Eqn. 3-9

To begin, we substitute Eqn. 3-3 into the right hand side of Eqn. 3-9:

$$P(T_s \leq t) = P(F_{T_k}^{-1}(R) \leq t)$$

Eqn. 3-10

We then apply F_{Tk} to both sides of the inequality, yielding:

$$P(T_s \leq t) = P(R \leq F_{T_k}(t))$$

Eqn. 3-11

We then make the observation that the probability that a uniformly distributed random number is less than or equal to a particular distribution is, in fact, the distribution itself. This observation and a substitution of Eqn. 3-2 yields the following result:

$$P(R \leq F_{T_k}(t)) = F_{T_k}(t) = P(T_k \leq t)$$

Eqn. 3-12

Computing the inter-arrival time reduces to a simple two step process:

- Uniformly choose R [0,1]
- Compute $F_T^{-1}(R)$ above (Eqn. 3-8)

3.6.2 Simulation Data

The MATLAB simulation was developed so as to study the general case in which the sewage system experiences both leaks and crew flushes. Since our model is based on the assumption that each flush instantaneously removes the same amount of pressure from the system and that a leak causes a pressure drop that is a linear function of time, a simple equation can be written to describe the system pressure, P_r, as a function of time. The general relationship describing the system pressure is

$$P_r = P_o - N\alpha_{flush} - t\alpha_{leak}$$

Eqn. 3-13

where P_r is system pressure, P_o is the high pressure set point, N is a discrete-valued random variable representing the number of flushes which have occurred up to a time t, α_{flush} is the amount of vacuum removed by a single flush, and α_{leak} is the rate at which the leak bleeds vacuum from the system.

The MATLAB simulation was operated using various flush and leak rates. Figure 3-10 presents a simulated histogram showing the distribution of time between pump runs for a no leak

case. This plot can be used as a baseline histogram to which all other simulated data can be compared.

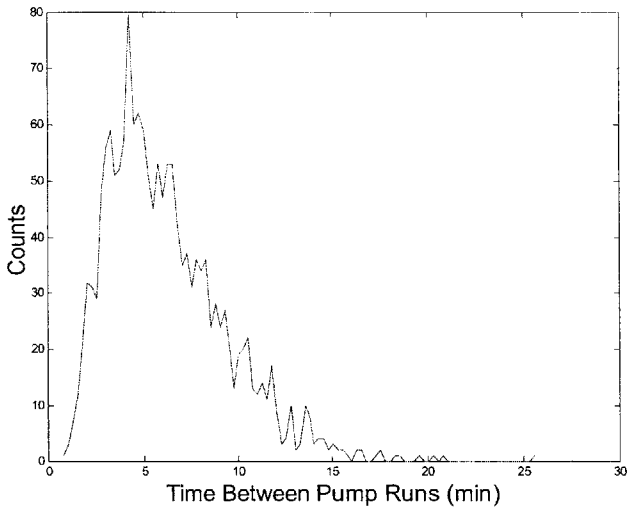

Figure 3-10: MATLAB simulation with no leak

The distribution of pump runs shown in Figure 3-10 resembles that formed from actual healthy system behavior as shown in Figure 3-6. As discussed in Section 3.5, this is expected because the flushing behavior used in the simulation was generated from the observations made aboard the ship. The similarities between these figures indicate that the sewage simulation can accurately describe the actual sewage system behavior, at least in the event that no leak is present. The system parameters used to generate Figure 3-10 are provided in Table 3-2.

Table 3-2: *SENECA* Sewage System Parameters

Parameter	Value
P_r	14 in/Hg
P_o	18 in/Hg
α_{flush}	1 in Hg/flush
α_{leak}	0 in Hg/hour
λ	0.66 flush/min

The no leak case can be further examined to demonstrate why the simulated no leak histograms appear as they do. Assuming there is no leak in the system, Eqn. 3-13 simplifies to:

$$P_r = P_o - N\alpha_{flush}$$

Eqn. 3-14

In order to determine the number of flushes, N_{max}, required to cause a pump run, Eqn. 3-14 is solved to find the value of the variable N that causes the overall system pressure to fall to the low pressure set-point. Thus, if the low pressure set point is P_{low}, then the value N_{max} is given by the relation:

$$N_{\max} = \frac{P_o - P_{low}}{\alpha_{flush}}$$

Eqn. 3-15

When using the parameters listed in Table 3-2, it is found that N_{max} is equal to 4 flushes. Thus, the distribution for the time between pump runs should resemble the shape of the Erlang PDF of order 4 for the value of lambda given in Table 3-2. A comparison of Figures 3-9 and 3-10 shows this to be true.

To consider the effect of a leak on the sewage system, first consider the case in which the only source of pressure drop is the leak. For this condition, Eqn. 3-13 can be simplified to:

$$P_r = P_o - t\alpha_{leak}$$

Eqn. 3-16

In this case, the time between pump runs must always be the same and that time can be calculated by solving Eqn. 3-15 for the time at which the system pressure, P_r, equals the low system pressure, P_{low}. Once the system reaches the low set point, it is true that the pressure

removed by the leak must exactly equal the amount of pressure removed by the occurrence of N_{max} flushes in the no leak case. For this reason, this time is denoted t_{Nmax}. Accordingly, it is possible to calculate a time t_i at which the leak has removed an amount of pressure equal to that which would be removed by i flushes, where i is an integer whose values lies between 0 and N_{max}, inclusive. This, t_i is given by the equation:

$$t_i = \frac{i\alpha_{flush}}{\alpha_{leak}}$$

The motivation for deriving the times t_i will become clear in ensuring presentation.

Now consider the most general case in which both flushes and leaks occur. Prior to arrival time t_1, it is true that the only scenario that can cause the pump to run is the arrival of N_{max} flushes. However if the pump has not run prior to the time t_1, but N_{max}-1 flushes have arrived by that point, then it is true that the combination of the pressure drop due to the leak and pressure drop due to N_{max}-1 flushes must cause the pump to run at t_1. This it must be true that in the more general case, the distribution for the time between pump runs must have a discontinuity at time t_1. The discontinuity is clearly illustrated in Figure 3-11.

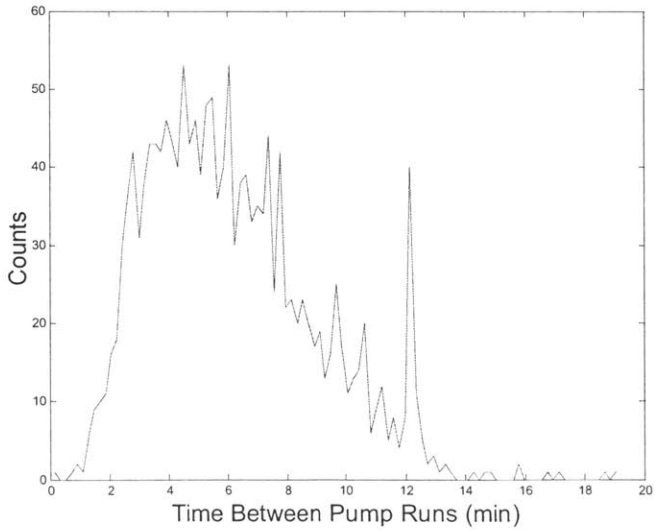

Figure 3-11: MATLAB Sewage Simulation with 5 in Hg/hour Leak

The simulation parameters used to generate Figure 3-11 are included in Table 3-3.

Table 3-3: Simulation Parameters

Parameters	Value
P_r	14 in./Hg
P_o	18 in./Hg
α_{flush}	1 in. Hg/flush
α_{leak}	5 in. Hg/hour
λ	0.66 in Hg./min

The location of the discontinuity in Figure 3-11 can be determined by solving for the value T_1:

$$T_1 = \frac{\alpha_{flush}}{\alpha_{leak}} = \frac{1}{\frac{5}{60}} = 12\frac{\min}{flush}$$

The rate of the leak rate will have a significant impact on the location of the discontinuity. For example, if we double the leak rate listed in Table 3-3 and run the simulation keeping all other parameters the same, a discontinuity is observed a 6 minutes as shown in Figure 3-12.

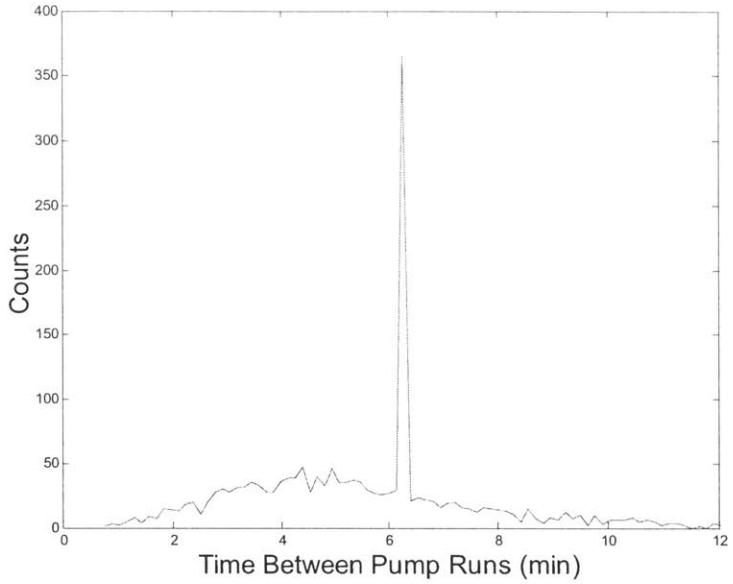

Figure 3-12: Simulation Data with 10 in Hg/Hour Leak

An updated calculation for T_1 confirms the location of this leak:

$$T_1 = \frac{\alpha_{flush}}{\alpha_{leak}} = \frac{1}{\frac{10}{60}} = 6\frac{\min}{flush}$$

Once we reach time T_1, the number of required flushes needed to cause the pump to run decreases by 1. For example, if the pump does not run prior to time T_2, and there have been exactly N_{max}-2 crew flushes prior to this time, the pump will run at T_2 since the leak has caused a pressure drop equivalent to that of 2 crew flushes. This type of logic can be extended to times through T_N.

In addition, we can also consider the interval between T_1 and T_2. In this interval, only N_{max-1} flushes are required to cause the pump to run because the leak has removed an amount of vacuum from the system equal to one flush. The pump could run on this interval if any of the following three conditions are satisfied:

- No crew flushes occurred before T_1 and N_{max}-1 flushes occur in the interval from T_1 to T_2
- 1 crew flush occurred before T_1 and N_{max}-2 crew flushes occur in the interval from T_1 to T_2
- 2 crew flushes occurred before T_1 and N_{max}-3 crew flush occurs in the interval from T_1 to T_2

Additional times at which the pump will run can be determined to N_{max}. For example we can predict a third possible time to see a discontinuity if the parameters are properly set as shown in Figure 3-13.

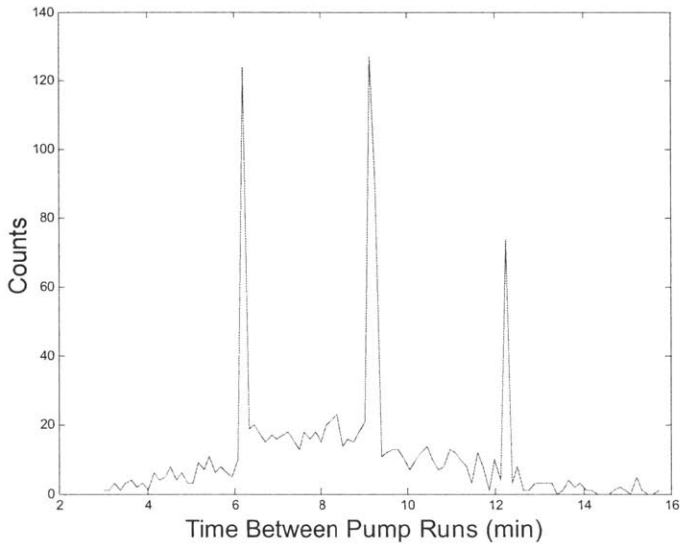

Figure 3-13: Simulation with lower flush drop

If we increase the leak rate and hold all other parameters steady, we still observe the presence of multiple spikes, but their relative location in the histogram has changed. If the leak rate increases, the time at which leaks will appear as flushes will decrease and cause a shift in the location of the spikes to the left. The expected time between pump runs shown in Figure 3-14 is approximately 3 minutes sooner than the pump runs occurred in Figure 3-13.

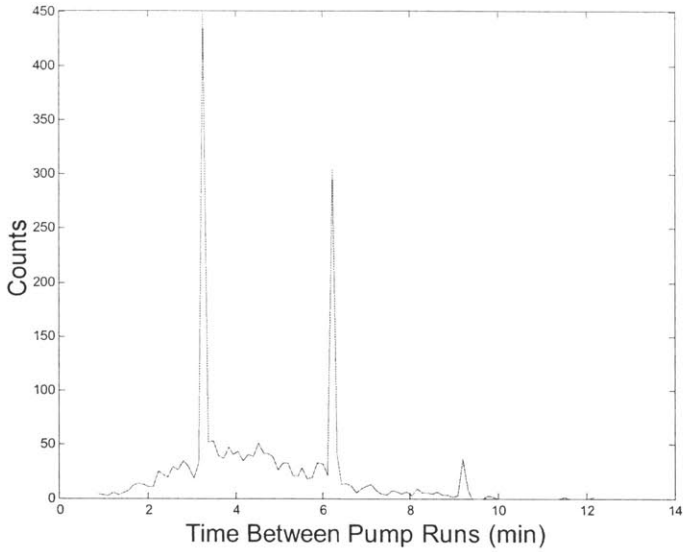

Figure 3-14: Simulation with large leak

3.7 Field Tests

In order to correlate the cycling of the vacuum pumps with a fault (i.e. a leak) in the sewage system, vacuum leaks of various sizes were inserted into the sewage system onboard SENECA. The vacuum leaks were controlled using a MATHESON TRI-GAS flow meter attached to the vacuum collection tank gauge line. In order to introduce a leak, the throttle valve on the flow meter was adjusted to achieve the desired flow rate. At least 30 hours of inport data was collected for each of 7 different leak rates. Actual sewage leak data appears as shown in Figure 3-15.

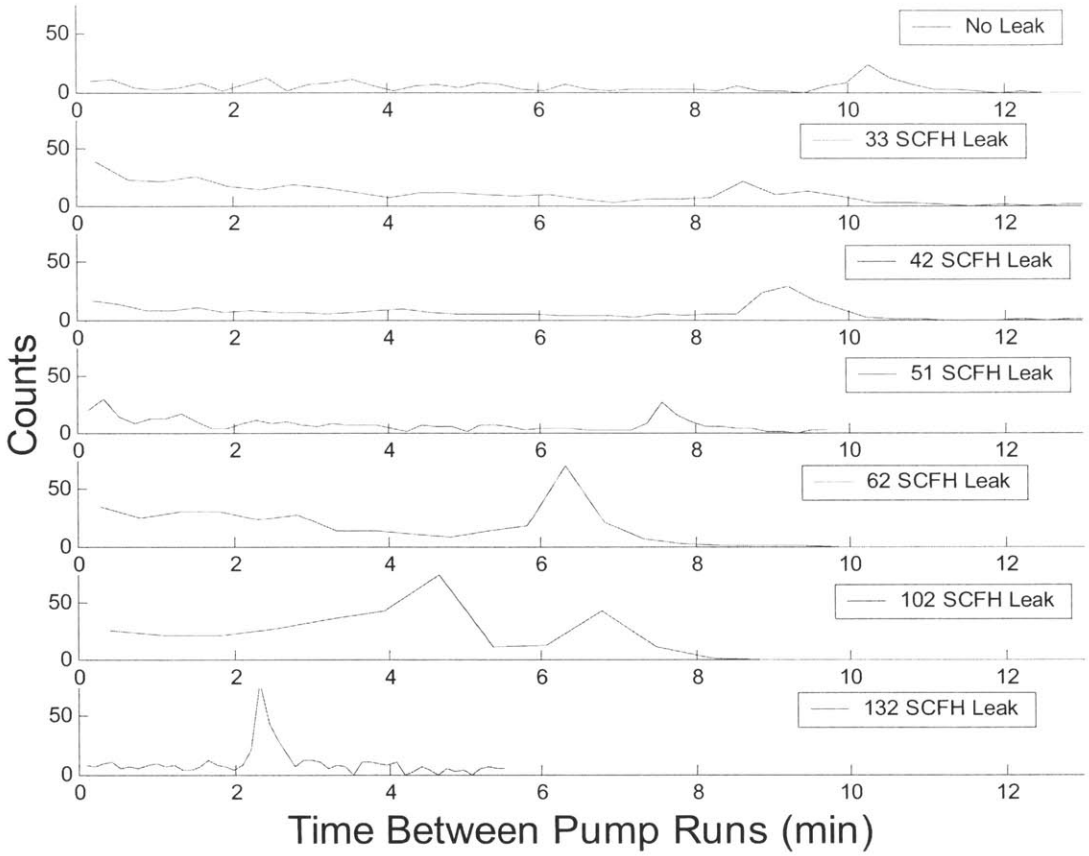

Figure 3-15: *SENECA* Leak Data

The sewage system data collected on *SENECA* displays trends consistent with those observed in the simulated data. Figure 3-15 illustrates seven different histograms collected in the presence of several different, known leaks. The histograms were generated using the MATLAB function hist and binned to 50 divisions. The small peak in the first "no leak" histogram in Figure 3-15 is probably due to a baseline loss in the vacuum system. As the rate of the leak increases, its associated peak is generally observed to grow in amplitude and to move to the left on the graph, indicating more frequent operation of the pumps. This is the same type of behavior that was observed in Figures 3-13 and 3-14. Our preliminary analysis indicates that the size and location of the peak can indicate both the presence and the extent of a system leak. A leak indicator can be developed from this type of histogram, which serves as a metric that indicates the possible presence and extent of a leak.

It is important to note that the baseline distribution for the time between pump runs shown in Figure 3-15 appears to follow neither the observed distribution plotted in Figure 3-6 nor the simulated distribution shown in Figure 3-10. This is reasonable, since Figure 3-15 was produced using inport sewage data instead of underway data. Despite this fact, our theory for how a leak manifests itself in the distribution for the time between pump runs still appears to be true. This makes sense, as the leak should cause a discontinuity in the distribution regardless of how crew flushes are distributed.

3.8 Diagnostic Indicator

In order to develop a diagnostic indicator for leak detection, a baseline no leak sewage histogram must be generated. Since the indicator will use peaks in the histogram to identify leak conditions, we must collect enough samples to detect the peak. Based on observed data trends, a minimum of 30 hours of data should be collected to generate practical histograms, especially when there is little or no leak in the system. Fewer samples may be required when the leak is large because the frequency of pump operation will be driven by the leak, not crew behavior. Additional study is recommended to determine a tighter lower bound for the number of samples needed in each case.

After the baseline data is collected, the NILM should monitor and compare subsequent sewage system trends to the baseline behavior. The location and movement of the peak in the newly generated histogram should be compared to the peak in the baseline data. The extent of this difference corresponds to the magnitude of the leak. It is important to note that the histograms must contain the same amount of data in order to determine relative peak heights; otherwise, a scaling factor must be applied to the data. To determine the scaling factor, a ratio between the number data samples is applied to the number of elements in each bin. For example, consider the case where we have two data sets, one containing 30 hours, the other containing 42. We would apply a scaling factor of 1.4 (42/30) to the smaller data set. This will account for the additional data that we would expect to observe had the data been collected for an additional 12 hours.

Chapter 4 Motor-Pump Coupling Analysis

4.1 Introduction

The Auxiliary Seawater (ASW) System on *SENECA* provides cooling water to vital shipboard loads such as the ship service diesel generators. Recently, the flexible coupling that connects the ASW motor to the pump has shown a tendency to fail prematurely (after approximately 8-13 motor starts). This is a maintenance burden because it requires the crew to frequently replace the coupling. Also, excessive coupling failure poses a risk of overheating machinery that can result in mechanical damage and reduced mission capability. This chapter presents how the NILM can be used to detect coupling failure in a motor-pump system.

4.2 System Description

The ASW system provides cooling for all heat loads onboard the ship other than those associated with the main engines. The system is designed to supply cooling water for numerous heat loads including the following: the ship's service diesel generators, hydraulic winch coolers, air conditioning condensers, waste heat condensers, stern tube and shaft seals, fin stabilizer hydraulic oil coolers, and other items. Suction to the two ASW pumps is taken through two supply lines from the bottom of the ship through a combination of suction screens, isolation globe valves, suction strainers, and butterfly valves. The isolation globe valves determine which suction is providing ASW cooling while the butterfly valves allow isolation of the strainers for cleaning. A butterfly valve across the inlets also allows cross-connecting the system to provide redundancy. Changing the flow rate is accomplished by throttling two butterfly valves at the outlets of the two pumps. For normal system operation, the overboard valve is throttled until a pressure gauge in the supply line for the heat loads shows a pressure of approximately 35 psig. Figure 4-1 shows a one-line diagram of the ASW system and Figure 4-2 shows a picture of the ASW motor and pump.

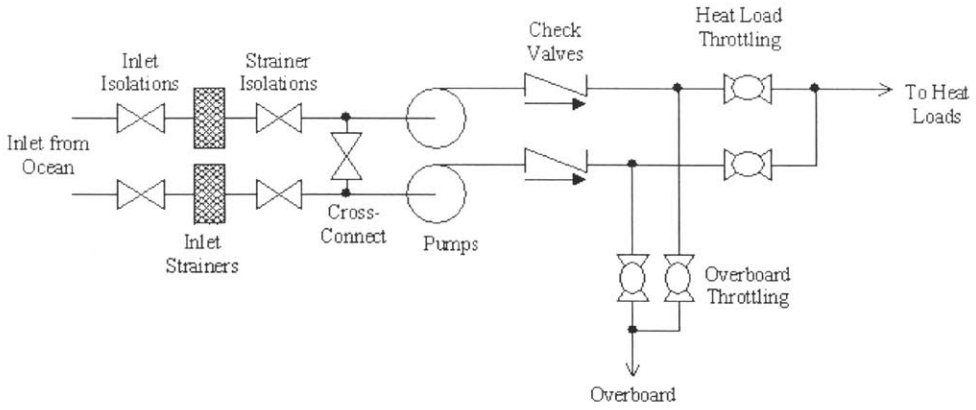

Figure 4-1: Diagram of *SENECA* Auxiliary Seawater System

The NILM installation for the ASW system uses one voltage transducer and two current transducers to monitor the pump motors. Specific component ratings and scaling factors are listed in Table 2.2.

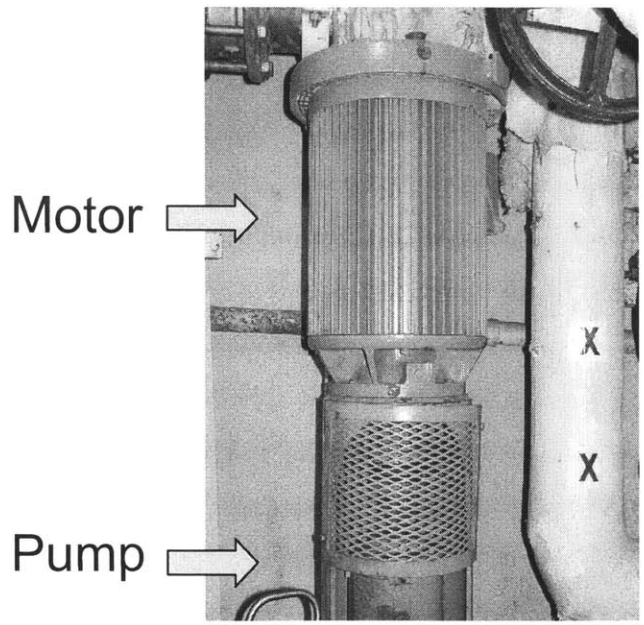

Figure 4-2: *SENECA* Auxiliary Seawater Pump and Motor

The *SENECA* uses a SURE-FLEX No. 6 coupling manufactured by T.B. Wood Sons Company to link the motor and pump in the ASW system. This coupling has a torque rating of

450 (in lbs.) and a stiffness of 1718 (in lbs. / rad) [19]. A picture of the coupling appears in Figure 4-3.

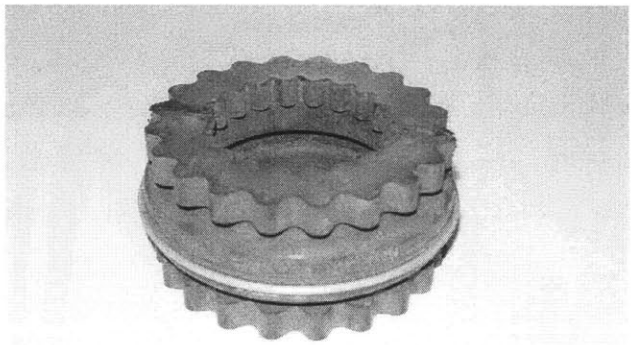

Figure 4-3: SURE-FLEX No. 6 Coupling

4.3 *SENECA* Coupling Failure Data

In order to investigate the effects of premature coupling failure a new coupling was installed and the NILM was configured to monitor the real power delivered to the pumps as the coupling gradually failed. Over the course of two days, the ASW system was manually cycled on and off to collect this data. An example of the ASW power data collected during a start appears as Figure 4-4.

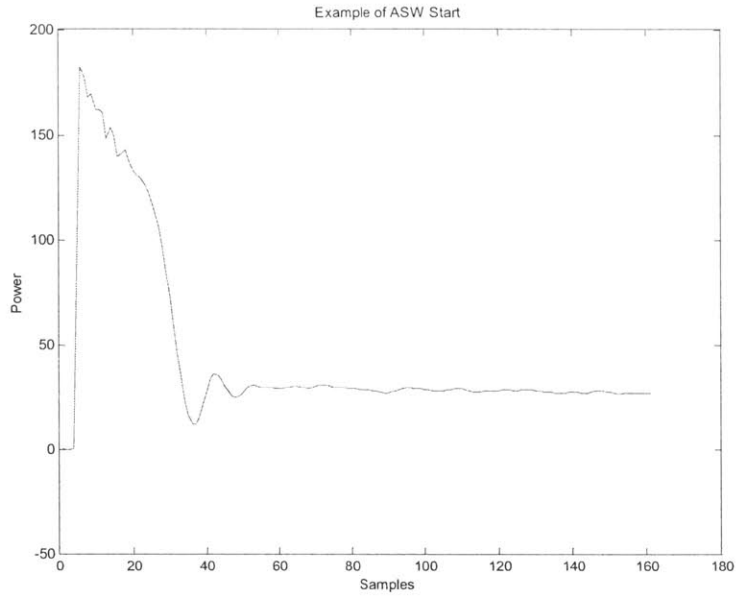

Figure 4-4: ASW Motor Start

When we compared the power plots from various coupling states to one another, we observed dramatic changes in the "ripple" of the transient. As the coupling progressively failed, the magnitude of the ripple in the transient increased. To isolate this trend, we calculated the frequency content of the transient power using the MATLAB spectrum and fft commands. The transient data was delineated as the first 30 data points after the peak of the real power trace. Using Figure 4-4 as a reference, it can be seen that this was a reasonable choice since steady state was achieved approximately 30 points after peak power was recorded. Due to the limited number of data points, the MATLAB command spline was used to interpolate the data. Figure 4-5 shows the frequency content of the transient during progressive deterioration of the coupling. A picture of the physical condition of the coupling at each state is also provided.

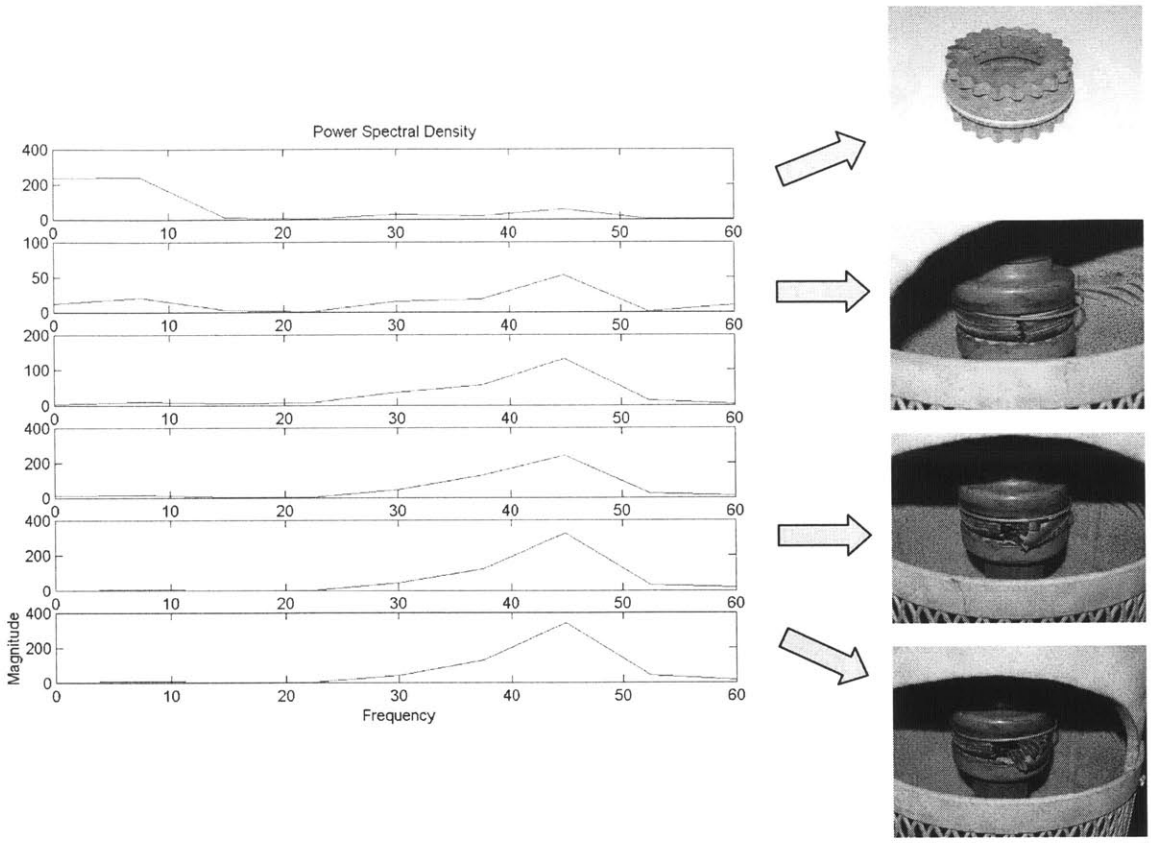

Figure 4-5: Frequency Content of Transient Power during Progressive Coupling Failure

The upper plot in Figure 4-5 shows the spectral density of the real power NILM trace of a healthy coupling. The presence of a nominal spike at about 43 Hz is characteristic of the ASW system. As the coupling progressively fails (each subsequent plot), the magnitude of the spike at 43 Hz increases until failure. To validate the trends observed in this data, coupling experiments were performed with an induction motor simulation.

4.4 Induction Motor Simulation

The starting transient behavior for large induction motors has been studied extensively [20]. A simulation is used in this chapter to explain observed behavior on the *SENECA*. The purpose of the induction motor simulation was to determine how the mechanical and physical parameters of the coupling affect the electrical properties of the motor.

4.4.1 Mathematical Model

Figure 4-6 shows a diagram of the mechanical system considered for the analysis conducted in this chapter. It represents the closest mathematical model that could be determined for the actual system. In this figure, a large squirrel cage induction motor drives an inertia load through an elastic coupling. For purposes of the simulation the coupling and spring are assumed to have negligible moment of inertia.

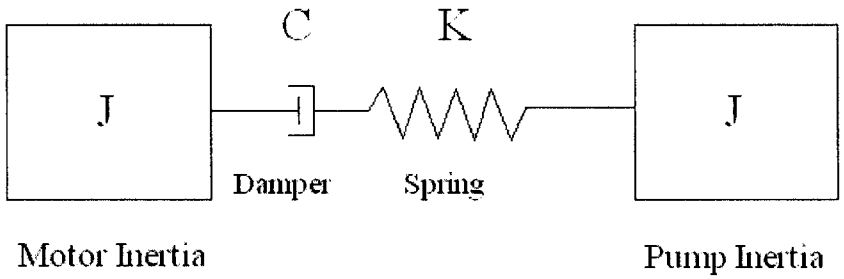

Figure 4-6: Mathematical Model of Auxiliary Seawater Motor Pump System

The computer simulation of the induction motor requires the simultaneous solution of the motor electrical state equations and the mathematical equations for the rotating mass-damper-spring system.

4.4.2 Electrical State Equations of the Induction Motor

The voltage and current equations of the induction motor can be represented in the d-q-synchronously rotating frame. The state equations of the basic 5th order induction motor model are as follows [21] :

$$\frac{\partial \lambda_{ds}}{\partial t} = \upsilon_{ds} + \omega \lambda_{ds} - r_s i_{ds}$$

$$\frac{\partial \lambda_{qs}}{\partial t} = \upsilon_{qs} - \omega \lambda_{ds} - r_s i_{qs}$$

$$\frac{\partial \lambda_{dr}}{\partial t} = (\omega - p\omega_r)\lambda_{qr} - r_r i_{dr}$$

$$\frac{\partial \lambda_{qr}}{\partial t} = -(\omega - p\omega_r)\lambda_{dr} - r_r i_{qr}$$

$$J\frac{\partial \omega_r}{\partial t} = \tau_e - \tau_l$$

Nomenclature for the variables of the induction motor state equations are presented below in Table 4-1.

Table 4-1: Induction Motor State Equation Variable Nomenclature

Term	Nomenclature
λ_{ds}	Direct axis stator flux
λ_{qs}	Quadrature axis stator flux
λ_{dr}	Direct axis rotor flux
λ_{qr}	Quadrature axis rotor flux
r_s	Stator resistance
r_r	Rotor resistance
i_{ds}	Direct axis stator current
i_{qs}	Quadrature axis stator current
i_{dr}	Direct axis rotor current
i_{qr}	Quadrature axis rotor current
v_{ds}	Direct axis stator voltage
v_{qs}	Quadrature axis stator voltage
ω	Frame speed
ω_r	Rotor speed
τ_e	Electromechanical Torque
τ_l	Load Torque

In order to take into account the effects of the coupling, the electrical state equations will be solved together with the mechanical equations that govern the mathematical system model presented in Figure 4-6.

4.4.3 Mathematical Equations of Rotating Masses

If torque is applied to a body that is free to rotate, the body will be accelerated in an angular direction and it will experience a change in angular momentum. Angular momentum is equal to the product of moment of inertia, J, and angular velocity Ω.

$$T = \frac{d(J\Omega)}{dt} = J\frac{d\Omega}{dt} = J\alpha$$

Eqn. 4-1

An ideal rotational damper contains no mass, and hence, the torque transmitted through it is undiminished during rotational acceleration. Therefore, the torque acting at its ends must always be equal and opposite. With a rotational damper there is no storage of retrievable mechanical work, as the work being done by an applied torque becomes dissipated as thermal energy. The relationship between torque and angular velocity is the product of a damping coefficient C and change in angular velocity Ω.

$$T = C[\Omega_1 - \Omega_2]$$

Eqn. 4-2

An ideal rotational spring stores potential energy as it is twisted or rotated and can be derived from Hooke's Law. Assuming the rotational spring has stiffness, K, the torque-displacement equation is:

$$T = K[\theta_1 - \theta_2]$$

Eqn. 4-3

All of the equations of the rotating masses, including the torsional dynamics of the mass, for the system in Figure 4-6 can be represented in terms of the angle of shaft rotation, θ, and angular velocity, ω:

$$\begin{bmatrix} \frac{\partial \omega_r}{\partial t} \\ \frac{\partial \theta_r}{\partial t} \\ \frac{\partial \omega_p}{\partial t} \\ \frac{\partial \theta_p}{\partial t} \end{bmatrix} = \begin{bmatrix} -\frac{C_c}{J_m} & -\frac{K}{J_m} & \frac{C_c}{J_m} & \frac{K}{J_m} \\ 1 & & & \\ \frac{C_c}{J_p} & \frac{K}{J_p} & -\frac{C_c}{J_p} & -\frac{K}{J_p} \\ & & 1 & \end{bmatrix} \begin{bmatrix} \omega_r \\ \theta_r \\ \omega_p \\ \theta_p \end{bmatrix} + \begin{bmatrix} \frac{1}{J_m} & \\ & -\frac{1}{J_p} \end{bmatrix} \begin{bmatrix} \tau_e \\ \tau_l \end{bmatrix}$$

4.4.4 Simulation Results

The ASW motors on *SENECA* are rated at 40hp and operate at a speed of 3550 rpm. The exact electrical parameters of the ASW motors could not be determined from the technical manuals and other documentation. These parameters could be obtained from direct measurements, but there was not sufficient time to do so. Thus, general parameters for a 50hp motor were used [22]. These parameters seem reasonable in this case and are listed in Table 4-2. Copies of the induction motor MATLAB simulation files appear in Appendix B. Simulated voltage and current (raw data) for the "A" phase of the induction motor appear as Figure 4-7.

Table 4-2: Simulation Motor and Pump Parameters

r_s (ohms)	X_{ls} (ohms)	X_m (ohms)	X'_{lr} (ohms)	r'_r	J (kg*m^2)
0.087	0.302	13.08	0.302	0.228	1.662

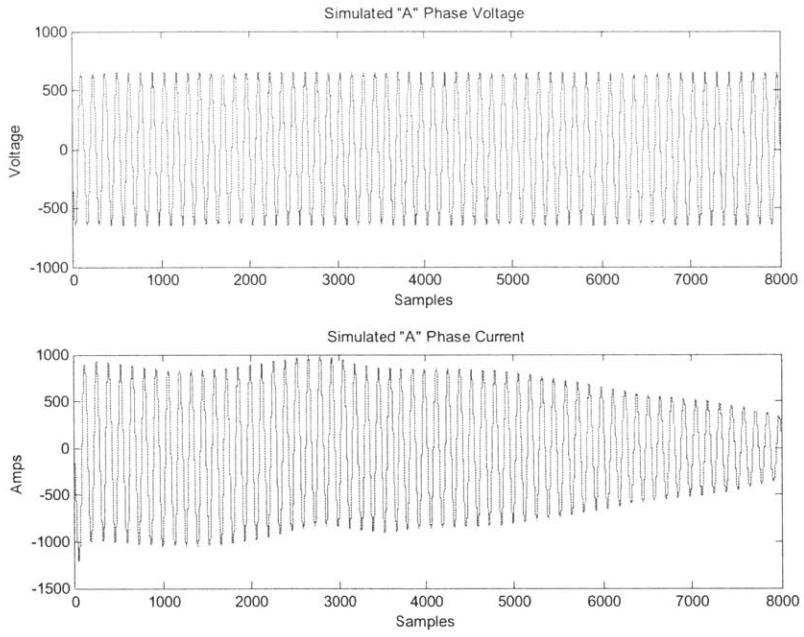

Figure 4-7: Simulated Induction Motor Voltage and Current

Since the deterioration of the motor-pump coupling clearly affects the frequency spectrum of the real power drawn by the motor, the study of the simulated data began by first examining the frequency content of the simulated real power. Initially, real power was computed by passing the voltage and current returned by the induction motor simulation to the NILM preprocessor for computation of the spectral envelope P_1. The spectral envelopes are sampled at a maximum frequency of 120Hz, which is normally more than sufficient for capturing the low-frequency variations that are typically observed in real and reactive power. In this case, however, the variations of interest are extremely close to the Nyquist frequency (i.e. one half of the sampling frequency), so the preprocessor samples them with relatively low resolution. Since the purpose of the simulation was to examine these high frequency components in great detail, it was decided to study the frequency spectrum of the instantaneous power rather than the frequency content of the NILM's P_1 spectral envelope. The total instantaneous power, defined in [21] as,

$$p(t) = v_A(t)i_A(t) + v_B(t)i_B(t) + v_C(t)i_C(t)$$

Eqn. 4-4

is sampled at the same frequency as both the simulated current and voltage. In this case, the simulation was designed so that the voltage and current were each sampled at 8 kHz. Thus, this signal should possess temporal resolution far superior to that which can be obtained with a spectral envelope. Moreover, the instantaneous power will contain at least as much spectral content as the P_1 spectral envelope. For these reasons, it was decided to examine the frequency content of the simulated total instantaneous power[2]. Figure 4-8 shows this waveform during the start of the simulated motor.

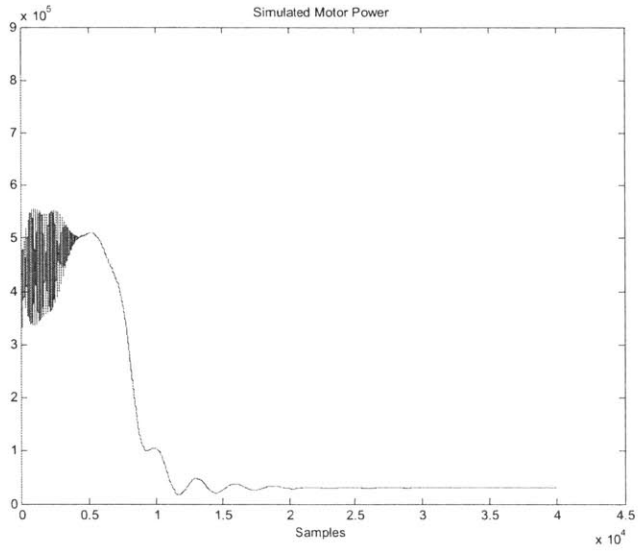

Figure 4-8: Simulated Motor Power

In order to understand the independent effects of the spring and damper, two separate simulations were conducted. The first simulation varied the value of the damping coefficient while keeping the spring constant value steady. The values for the damping coefficient, varying in the simulation from 0 to 2 in increments of 0.5, were chosen based on recommendations from the coupling manufacturer [19]. The frequency content of the transient power was examined in

[2] Although the total instantaneous power provides excellent temporal resolution, it does not have the same interpretation as the spectral envelope P_1. In the future, it would be worth considering the possibility of producing spectral envelopes with greater temporal resolution. This is, after all, possible since the spectral envelopes could be calculated at the same rate as the voltage and current. Alternatively, a simplistic but far less informative approach would be to interpolate the 120Hz spectral envelopes. This approach, though appealing, does not elucidate any information that is not already contained in the spectral envelopes as they are currently computed.

each case. For the purposes of these experiments, the transient was defined as the first 1800 points of the instantaneous power. Instantaneous power was calculated using Eqn. 4-4 and filtered using an 1800 point Hanning Window. The frequency spectrum was then calculated using an 1800 point Fast Fourier Transform (FFT).

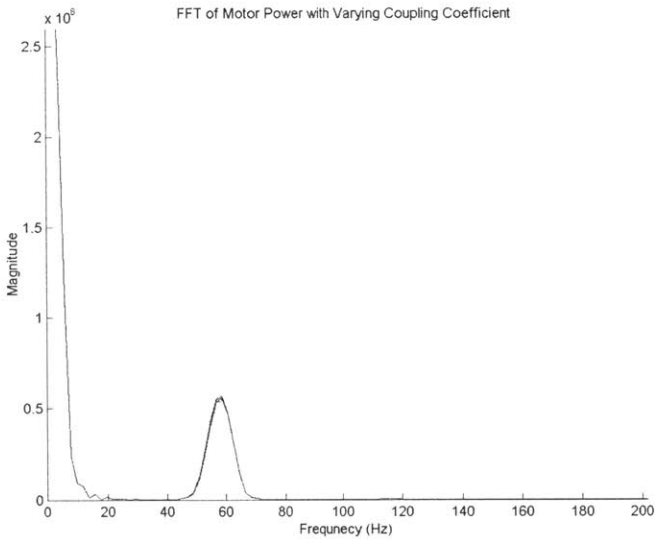

Figure 4-9: ASW Magnitude Varying Coupling Coefficients

Figure 4-9 illustrates that the health of the coupling is manifested in the electrical power of the motor. As the coupling deteriorates, the magnitude of the power increases around 58 Hz (slip). In order to observe the changes in this magnitude, the 54-64 Hz region of the power spectrum is magnified and shown in Figure 4-10.

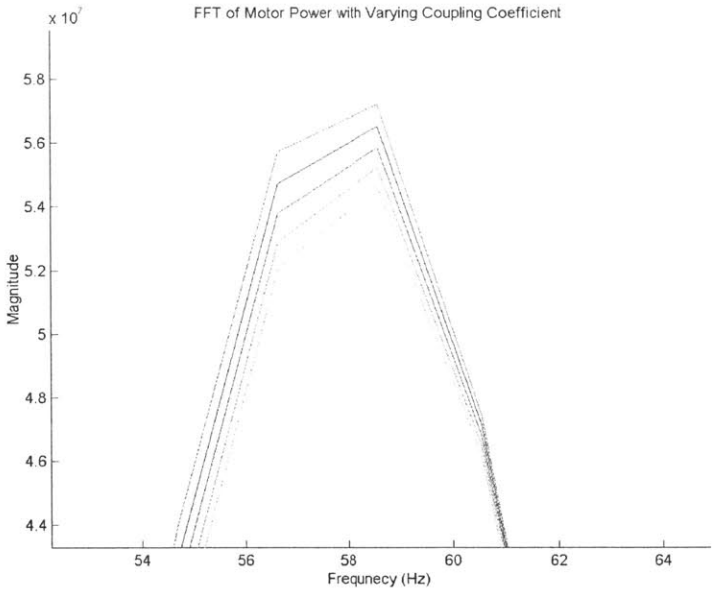

Figure 4-10: ASW Magnitude Varying Coupling Coefficients (54-64Hz)

Figure 4-10 illustrates the change in the magnitude of pump power with a varying coupling coefficient. As the coupling deteriorates, the magnitude of the power increases. A system with a coupling coefficient of 2 requires less power than a coupling coefficient of 0 (no coupling).

In order to observe the effects of the spring on this system, a second simulation was performed where the spring stiffness was varied from 0 to 200 in increments of 50 while the damping coefficient was held constant at a value of 0.5. The frequency spectrums of these experiments appear as Figure 4-11.

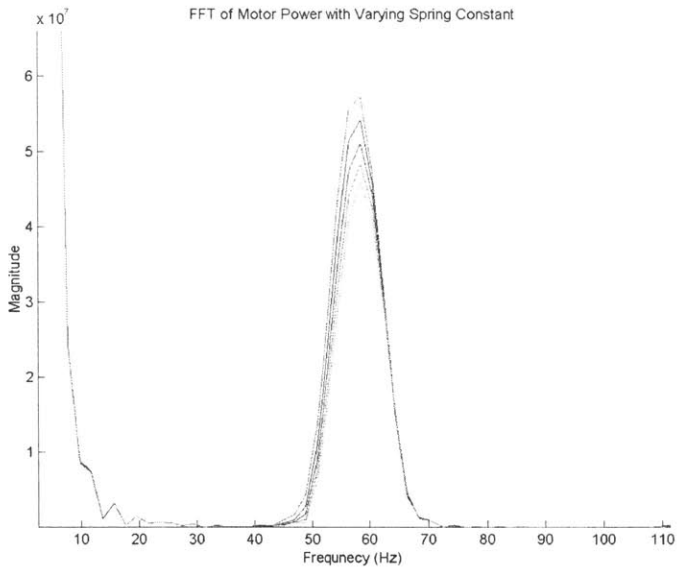

Figure 4-11: ASW Magnitude Varying Coupling Stiffness

Figure 4-11 demonstrates that the health of the coupling is also manifested by a change in the stiffness of the spring. As the coupling loses stiffness, the magnitude of the power again displays an increase around 58 Hz (slip). Figure 4-12 shows the magnified 54-64 Hz region of the spectrum to better illustrate the progressive deterioration of the coupling.

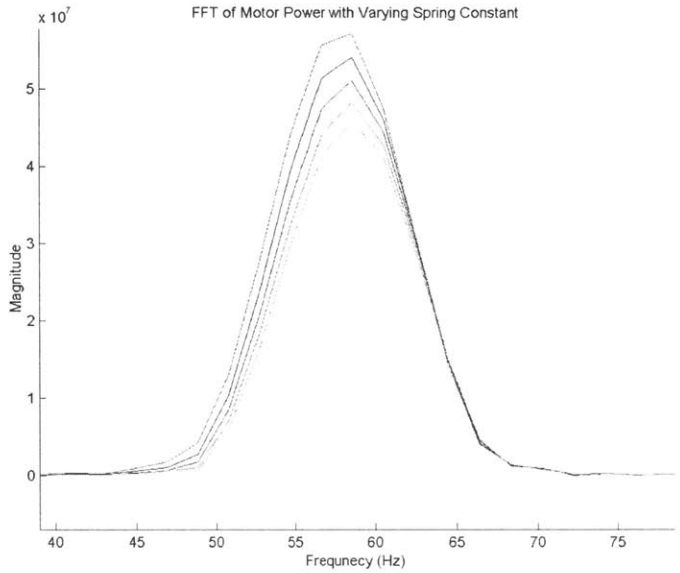

Figure 4-12: ASW Magnitude Varying Coupling Stiffness (40-75Hz)

The locations of the peaks in simulation Figures 4-10 and 4-12 (58 Hz) differ from the location observed in the actual coupling (42 Hz), but this is expected since we are not using the actual ASW motor pump parameters in our simulation.

Using a full factorial design, one by which every setting of every factor appears with every setting of every other factor, the combined damping and stiffness effects on the magnitude of the FFT in the 50-70 Hz range is presented in Figure 4-13.

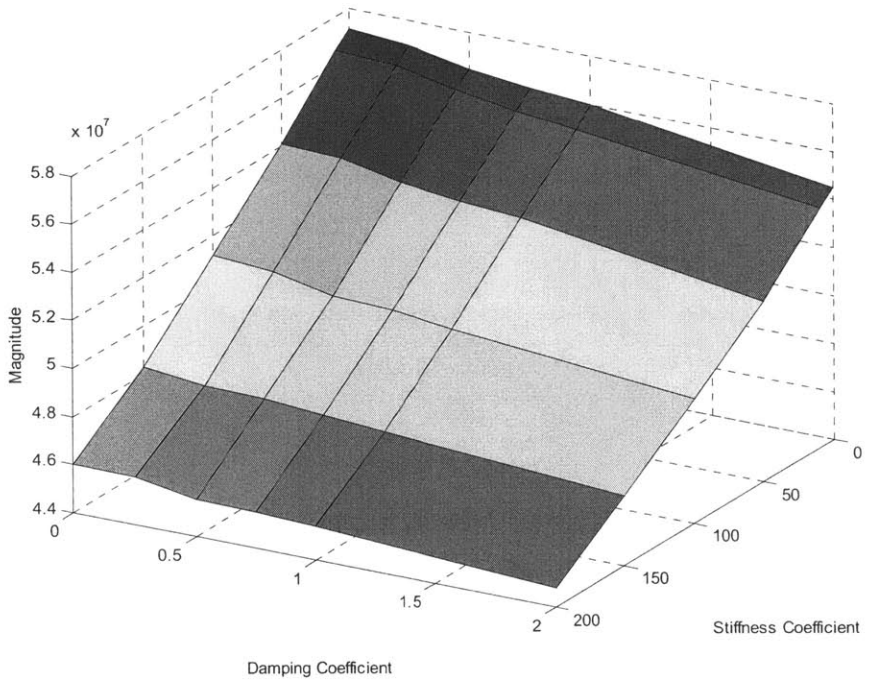

Figure 4-13: Joint Effects of Coupling Coefficient and Stiffness on Power Magnitude

The steeper slope of the graph along the stiffness coefficient axis indicates that this parameter has a larger impact on the magnitude of power over the range of values it was tested. Although the damping coefficient impacts the magnitude of the power, the variation in coupling stiffness appears to be a better indicator of coupling health.

4.5 Improper Coupling Selection

The rapid failure of the coupling in the ASW system may indicate an improper coupling size and/or improper stiffness and damping coefficients. In the case of electro-mechanical systems, proper coupling size and stiffness is extremely important. If the coupling is too stiff, it offers reduced machine protection, i.e., the machine may damage itself before the coupling fails. On the other hand, if the coupling is not stiff enough, it may be subject to premature failure.

One of the key contributors to premature coupling failure is the angle of deflection of the coupling. A simulated example of hypothetical coupling deflection appears below in Figure 4-14.

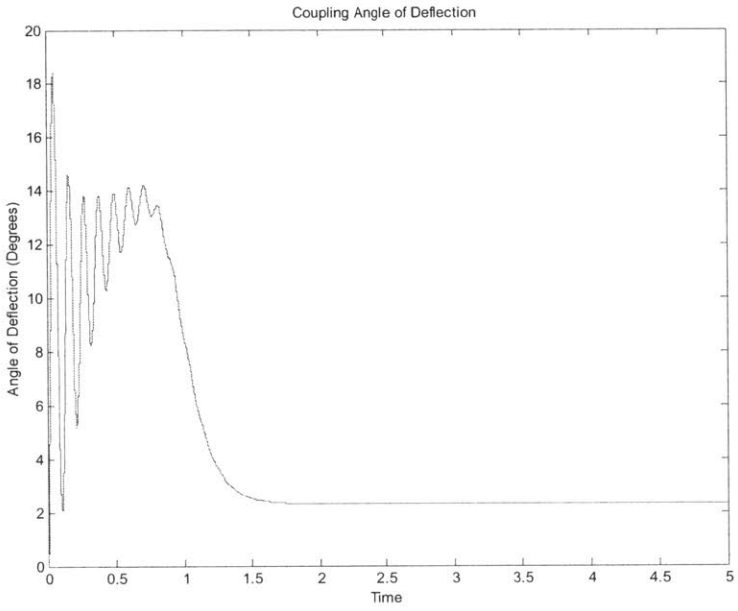

Figure 4-14: Simulated Coupling Deflection Angle

In Figure 4-14, a maximum deflection of 18° is observed at initial start-up before the coupling settles to permanent deflection of less than 3°. In this example, the values for coupling coefficient and spring constant are hypothetical, although quantitatively they are much higher than the No. 6 SURE-FLEX coupling used on *SENECA*.

If the actual coupling damping coefficient and spring stiffness constant from *SENECA's* coupling is used, a mach larger angle of deflection is observed, as illustrated in Figure 4-15.

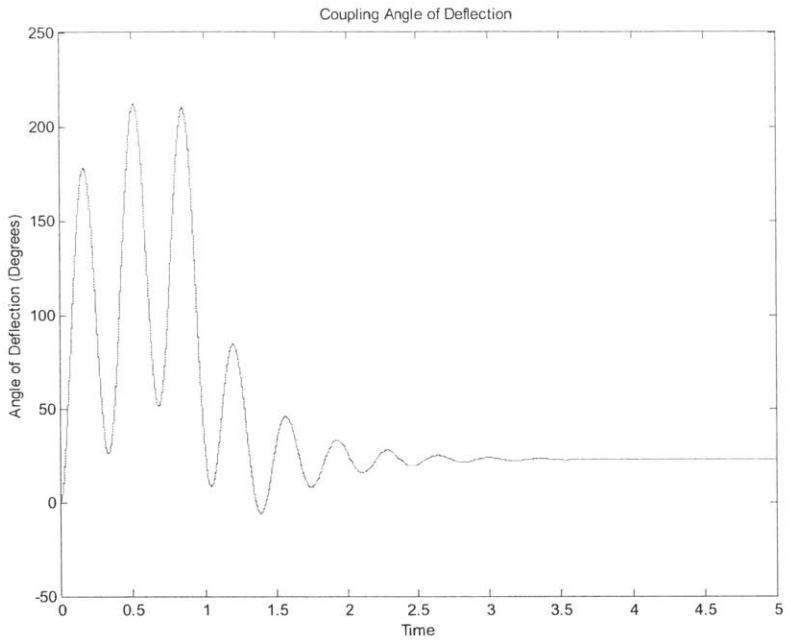

Figure 4-15*: SENECA* Coupling Deflection Angle

The extremely high angle of deflection at start-up and the high value of steady state deflection may indicate the coupling is improperly sized. The maximum allowable angle of deflection on *SENECA's* coupling is 15^{o} [19]. The deflection value observed in Figure 4-15 is well beyond the manufacturer's suggested angle of deflection for the coupling and is probably one of the key contributing factors to premature failure. It is important to note that the behavior of the deflection angle in the actual ASW system may not be exactly as it is shown here. Without the actual motor parameters, it is difficult to know for sure. All that is attempted to show here is one possible method of failure which is consistent with observed data and manufacturer's ratings.

In order to test this hypothesis, a new Hytrel coupling with higher damping and stiffness coefficient was installed on *SENECA's* ASW system. This new coupling has a rated torque of 1800 (in lbs.) and a stiffness of 10000 (in. lbs./rad). In essence, it is five (5) times stiffer than the coupling *SENECA* currently uses. A picture of the coupling appears as Figure 4-16.

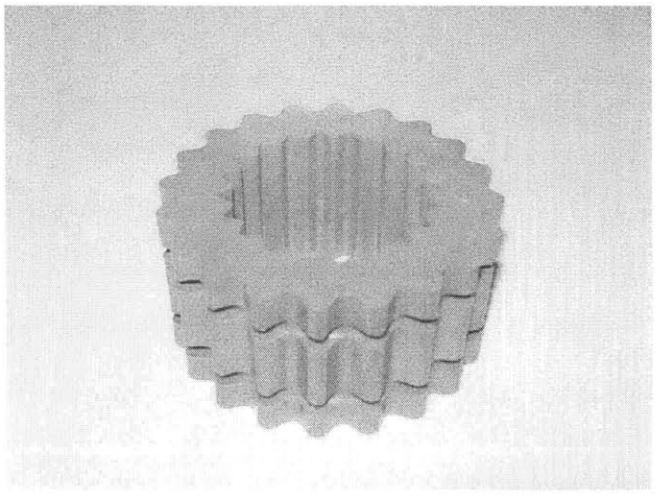

Figure 4-16: Hytrel Sleeve Coupling

With the new coupling installed onboard the ship, 127 consecutive motor starts were captured with the NILM. The spectrum of the real power transient measured by the NILM on the 127th start appears below as Figure 4-17. The absence of electrical variation or spike throughout the frequency range (with the exception of the DC offset) in this figure indicates that this coupling is properly performing and displays no outward signs of wear and/or deterioration. A visual inspection of the coupling showed no cracks, tears or other indications of excessive wear or fatigue.

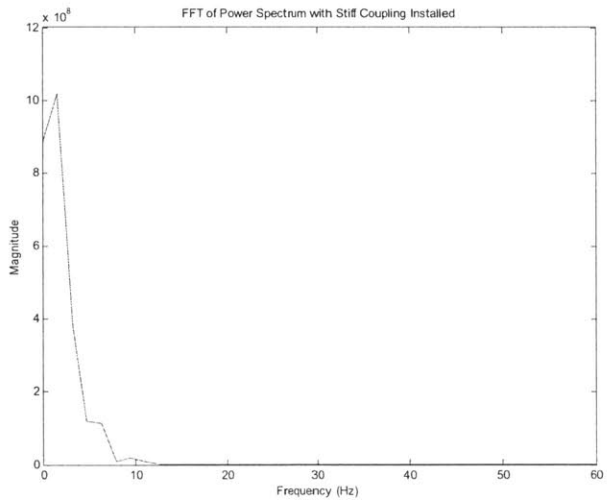

Figure 4-17: *SENECA* ASW Power Spectrum with Hytrel Coupling

It would appear that the previous coupling currently used onboard *SENECA* is not stiff enough for the application. The stiff Hytrel coupling reminded many crew members of the "old ceramic" coupling the ship once used on this system [23]. After installing the Hytrel coupling on the cutter, no coupling failures have been recorded.

4.6 Diagnostic Indicator

There are numerous methodologies that could be employed to successfully diagnose a coupling failure. The key indicators of coupling failure are the magnitude and location of the spike in the power spectrum of the coupling. Unfortunately, the frequency location of the spike, and to some extent its magnitude, is dependent on both the system and coupling characteristics; there is no universal solution to this problem.

To develop a coupling failure diagnostic indicator, one should begin with observation and identification of the frequency band where coupling failure is manifested. Once this frequency band is identified, a band pass filter can be used to monitor this window of data. Once the magnitude of power in this band reaches a predetermined failure threshold, the coupling should be replaced. Although the frequency band will have to be identified and customized for each system, it is expected that identical systems on a class of ships would have the same identifying limits and parameters.

Chapter 5 Fluid System Blockage

5.1 Introduction

An unexpected underway overheat of *SENECA's* number one ship service diesel generator (SSDG) provided a unique opportunity to observe the effects of obstructions in the fluid system. While underway on routine patrol, *SENECA* secured the number one SSDG due to overheating. Marine growth in the end bells of the SSDG lubricating oil cooler restricted water flow to the cooler. The lack of cooling water caused a temperature rise in the SSDG. Marine growth obstruction is a problem that commonly plagues ships that transit from cold to warm water. In most cases, mussels grow in the end bells of the heat exchangers while the ship is in cold water. They then detach themselves in warm waters, blocking the tube passages of the heat exchanger, ultimately causing a reduction of flow through the heat exchangers.

The heat exchangers represent a relatively small, but absolutely critical, section of the ASW system. The fundamental question is whether a crippling blockage in a small branch of the system piping will influence the average power consumed by the ASW pump. To attempt to detect flow restrictions, fluctuations in the real power drawn by the ASW pump were examined. This chapter investigates the impact of flow restrictions in a piping system and considers whether pressure oscillations caused by irregularities in the flow can be detected in the pump electrical signature.

5.2 System Description

An overview of *SENECA's* ASW system has already been provided in Chapter 4. A line diagram of the system appears as Figure 4-1. In order to prevent overheating of the SSDG's, the Coast Guard reconfigured the ASW piping. In the old configuration, engine cooling freshwater was cooled directly from the ASW system through the heat exchanger. If ASW water flow was restricted, the capacity of the engine cooling water to absorb the heat load was very limited. In addition, the location of the heat exchanger on the side of the engine made it very difficult to

access for cleaning purposes. In the new piping configuration, an additional freshwater loop has been installed and the heat exchanger was relocated to a more accessible position.

5.3 *SENECA* Casualty Data

Frequency domain analysis has shown that certain loads do not consume power at a steady, unchanging level, even during nominal operating conditions. In a fan, for example, aerodynamic fluctuations and wind can cause rapid fluctuations in the real power consumed by a fan motor [24]. In a fluid pumping system, it is possible that mechanical resonance in the piping system results in a modulation of the pump motor load current. Speculatively, such effects may manifest as higher frequency fluctuations in the real power consumption of the motor.

In the case of the ASW pump, the frequency spectrum of the real power drawn immediately prior to the overheating episode was compared to the frequency spectrum of the real power drawn immediately following the pump's return to operation after cleaning approximately two hours later. The difference in the frequency spectrums are shown below as Figure 5-1.

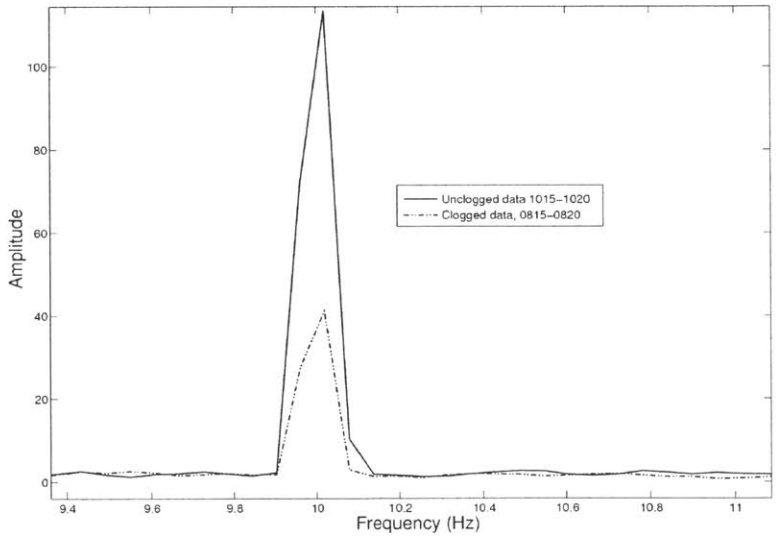

Figure 5-1: Frequency Spectra during *SENECA's* Heat Exchanger Overheat

In figure 5-1, a 10Hz variation in the amount of real power drawn by the pump is observed. In addition, the magnitude of this variation became significantly reduced once the generator became clogged. Since the ship's logs indicate that the only component in the ASW system whose

temperature increased prior to the overheating incident was the number one SSDG, it seems likely that the change in the magnitude of the 10Hz variation was due to the blockage there.

5.4 Fluid Test System

In order to investigate the effect of pressure oscillations in the electrical power of the motor, a Setra Model 230 Wet/Wet Differential Pressure Transducer was installed on the fluid test system in the lab. The motor in this system is rated at ½ horsepower and operates at 3450 RPM (60Hz, 450 volt). The pump impeller has 6 blades. A line diagram of this system appears as Figure 5-2.

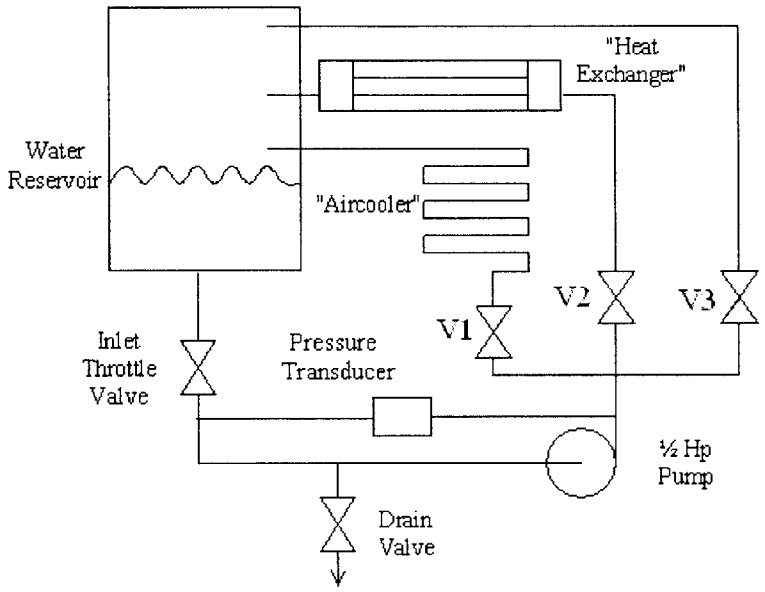

Figure 5-2: Line Diagram of Fluid Test System "BRUTE"

The pressure transducer is designed to sense a differential pressure across the pump inlet and outlet and convert the difference in pressure to a proportional high level analog output. The Setra model 230 provides either a 0 to 5 VDC or 0 to10 VDC voltage output or a current output of 4 to 20 mA. Electrical connections are made through top cover of the transducer. A picture of the pressure transducer appears as Figure 5-3.

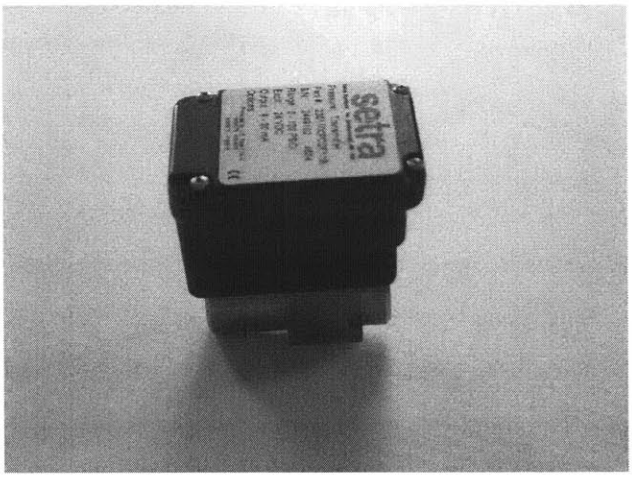

Figure 5-3: SETRA Pressure Transducer

5.4.1 Data Acquisition Technique

In order to capture voltage, current and pressure data simultaneously, the transducer was configured to collect data in tandem with the NILM. Since the A/D converter requires a voltage to operate, the current output from the transducer was placed across a resistor in order to achieve a proportional voltage measurement. The NILM computer was then able to record to the pressure voltage on a third input channel with only minor modifications to the system configuration files. The following LINUX command was used to configure the PCI card to read the third channel:

```
set1710 –d/dev/pci1710 < threechannelcfg.pci
```

To collect raw data with all three channels, the following command is employed:

```
dd if=/dev/1710/pci1710 | pci2asc > filename
```

Once the raw data is captured, it must be processed to create power envelopes. The following command is used to accomplish this:

```
cat filename | chansift2_12bit_pl 1 2 | prep stdin –p ~/bin/prep_musfp_txt.so > filename
```

Once the power files are created, they can be burned to CD using the method and LINUX commands outlined in [9].

Since raw data was also collected on third channel, we must convert it from quantized data into a system pressure. To convert the transducer output to a pressure value we must scale the A/D converter output to a voltage that ranges from +5 to -5 volts. Since the A/D converter quantizes data into values that range between 0 and 4096, the appropriate conversion equation is:

$$V_{SETRA} = \frac{10}{4096}(V_{in} - 2048)$$

Eqn. 5-1

To convert the transducer voltage to a current, the voltage in Eqn. 5-1 is divided by the value of the resistor it was measured across:

$$I_{SETRA} = \frac{V_{SETRA}}{R_{NILM}}$$

Eqn. 5-2

From the current, the pressure can be determined directly using the following equation [25]:

$$PRESSURE = \frac{(I_{SETRA} - 0.004) * 50}{0.016}$$

Eqn. 5-3

5.4.2 Fluid Test System Clogging Scenarios

In order to imitate the progressive clogging or blocking of a heat exchanger, laboratory experiments were conducted at four different clogging levels. In addition to the unblocked or unclogged condition, data was captured for three other blocked-tube conditions. The different modes of heat exchanger blocking are illustrated in Figure 5-4.

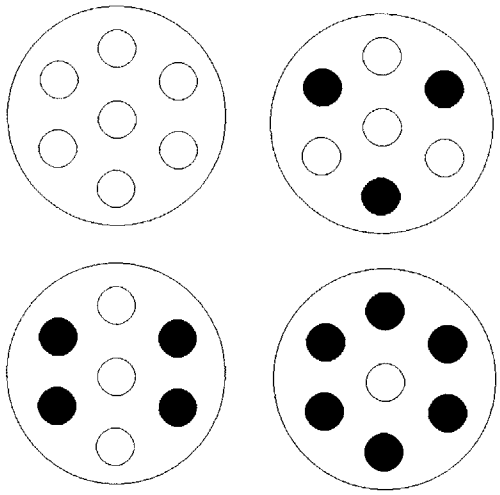

Figure 5-4: Fluid Test System Clogging Schemes

5.5 Experimental Results

Since power and pressure data may be extremely sensitive to changes in the piping configuration, two different flow paths were considered in this experiment. In the direct fluid flow path, water exiting the pump cavity flows directly through the heat exchanger. The branch lines to the air cooler and water reservoir are shut. In this type of piping arrangement, flow restriction and pressure oscillations can not be absorbed by the additional flow path, and may have a greater likelihood of being observed in the electrical signal of the motor. In the indirect fluid flow path, water exiting the pump not only flows to the heat exchanger but can also return to the water reservoir through dedicated piping. In this multiple path flow arrangement, restriction caused by the blocked heat exchanger could be absorbed by the other flow paths.

5.5.1 Direct Fluid Flow Path

In the case of the direct fluid path, water from the pump discharge flowed directly through the heat exchanger by opening valve V2 in Figure 5-2. Valves V1 and V3 were closed. In this arrangement, no alternate fluid flow paths were available. An example of the real power data collected by the NILM in the unclogged case appears as Figure 5-5.

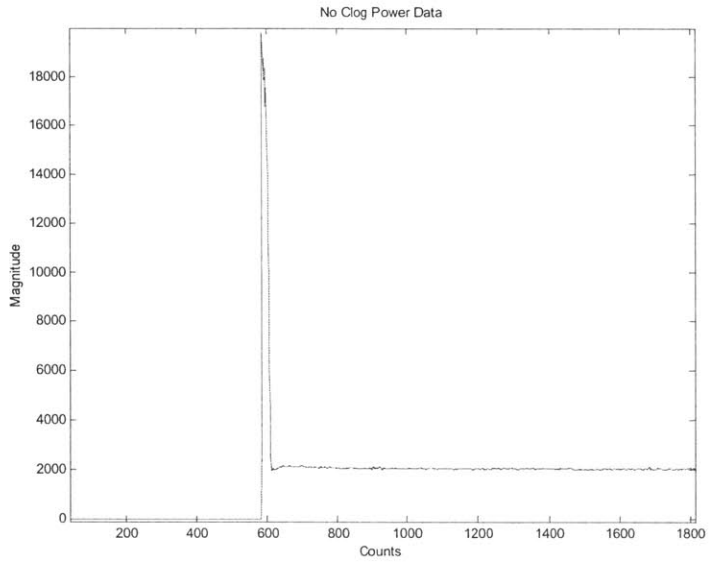

Figure 5-5: Real power collected by the NILM in the unclogged condition

The frequency content of the real power was calculated using the spectrum command in MATLAB. The spectral density for each of the four clogging cases is presented as Figure 5-6.

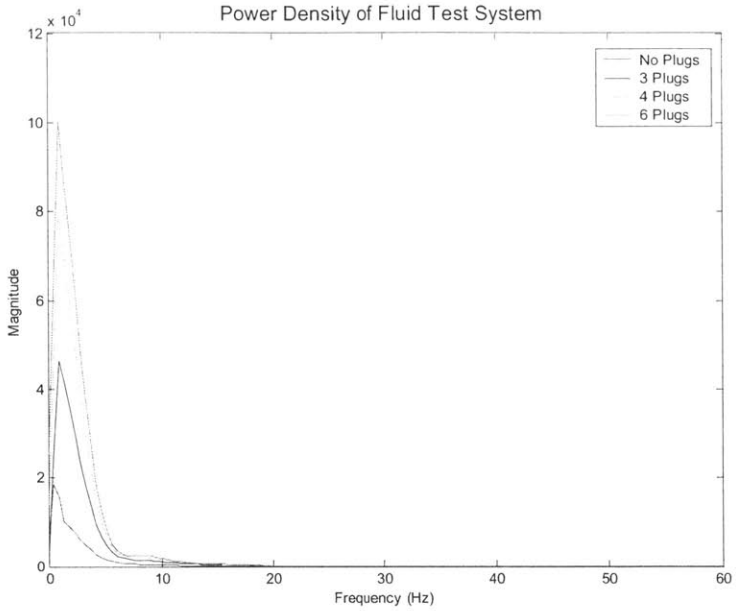

Figure 5-6: Frequency Spectra of Real Power for the Fluid Test System during Different Levels of Clogging

Figure 5-6 indicates that there is little oscillation in the electrical frequency of the pump motor. It is important to note that the magnitude of pump power increases in a linear fashion with increased clogging or flow restriction. The largest magnitude of power density was observed when the heat exchanger was clogged with 6 plugs. Surprisingly, this trend contradicts the *SENECA* blockage data presented in Figure 5-1. In this case, the magnitude of the power oscillations increased with blockage while they decreased with blockage in Figure 5-1. The frequency content of the pressure data for the direct fluid flow path is shown as Figure 5-7.

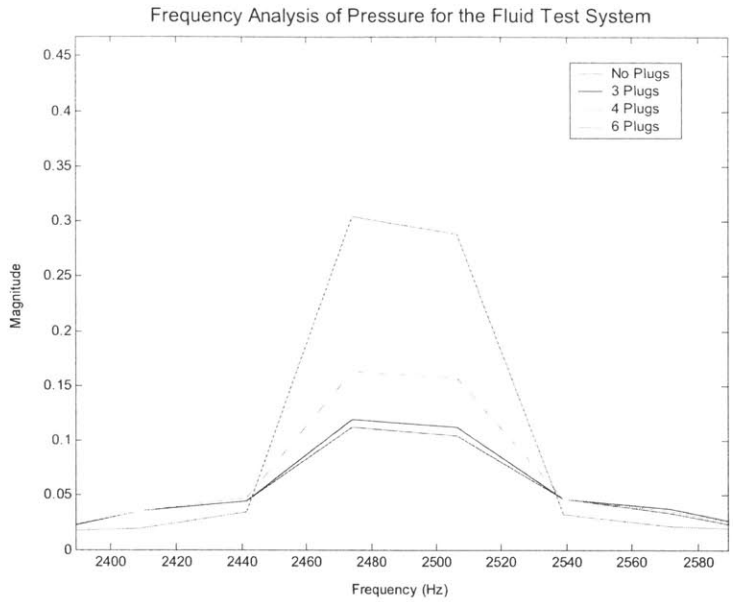

Figure 5-7: Frequency Spectra of the Pressures during Different Levels of Clogging

Figure 5-7 indicates that as the heat exchanger becomes more and more clogged, there is also an increase in the pressure oscillations at some factor of the electrical frequency and blade count of the pump. Again, the largest magnitude in the pressure fluctuation was observed when the heat exchanger was clogged with 6 plugs. A combination of the results in Figures 5-6 and 5-7 would indicate that the electrical power oscillations are in some manner proportional to the pressure oscillations.

5.3.2 Alternate Fluid Flow Path

Unfortunately, most shipboard cooling systems are not designed with exclusive flow routes to each piece of equipment. Most often, cooling water flows through a main header off of which line braches cool different loads. The same experiment was now run with an alternate fluid flow path open for the pump to account for this engineering practice. In this configuration, valves V2 and V3 in Figure 5-2 were opened while valve V1 remained closed. Again, the power spectral density for each of the four cases with an alternate fluid flow path were computed using the spectrum command and are shown below in Figure 5-8.

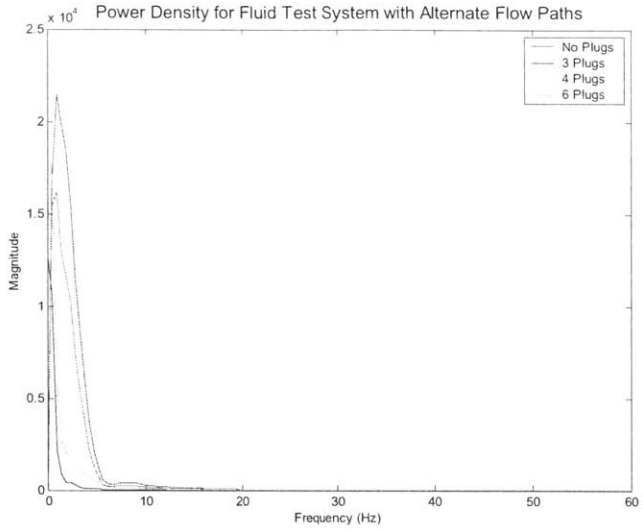

Figure 5-8: Frequency Spectra of Real Power for the Fluid Test System during Different Levels of Clogging using Alternate Flow Paths

Unlike the previous direct path flow experiment, Figure 5-8 indicates that increased blockage in the fluid system results in smaller magnitude of electrical oscillation. In this case, the largest magnitude of the power density was achieved with an unclogged (no plugs) heat exchanger. The trends observed in this data agree better with those observed in Figure 5-1.

The spectrum of the pressure data with alternate flow paths indicates a similar trend to that observed in Figure 5-8. As the heat exchanger becomes more and more clogged, the pressure modulation subsides. The data for this case is shown in Figure 5-9.

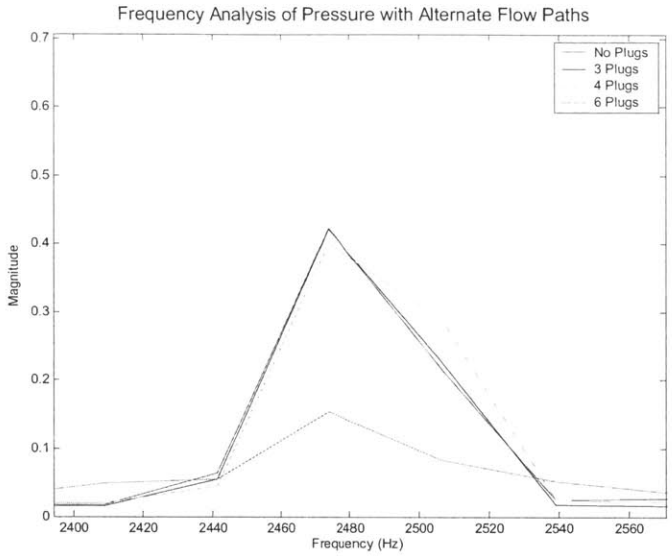

Figure 5-9: Frequency Spectra of the Pressures during Different Levels of Clogging using Alternate Flow Paths

5.6 Conclusion

In a direct flow path scenario, flow restriction and blockage cause an increase in the magnitude of power and pressure oscillations. The magnitudes of these oscillations appear to increase with the amount of system blocking. This is not true when we have a system where there are multiple branches or flow paths in the piping. In these cases, the data illustrates a mixed and somewhat opposite effect. The oscillations normally expected in the direct flow scenario seem to be absorbed by the additional flow paths and the magnitudes of the oscillations are dampened. The frequency domain analysis of the ASW system data in this chapter suggests that the clogging of a heat exchanger on a critical shipboard system can be identified with the NILM, although the extent of diagnosis is dependent on the system flow patterns. Because a ship has many different flow paths, detection using power and pressure oscillations are not advisable.

Chapter 6 *SENECA* Reverse Osmosis System

6.1 Introduction

There are a variety of ways a ship at sea can produce fresh water from saltwater. One method is by the evaporation of seawater. In this technique, seawater is boiled to produce steam; the steam is then captured and condensed. The resulting condensate contains virtually no impurities. Unfortunately, this type of system is energy intensive and is very difficult to maintain. Recently, the *SENECA* converted from the evaporator type system to the reverse osmosis type system. This chapter discusses the reverse osmosis process, explains the installation of NILM's in the system and presents preliminary data results.

6.2 Reverse Osmosis

Reverse Osmosis (RO), like many other practical scientific methods, has been developed from processes first observed in nature. Osmosis is a naturally occurring phenomenon in which a semi-permeable membrane separates a pure and a concentrated solution (a semi-permeable membrane is defined as one that preferentially passes a particular substance). Every fluid has an inherent potential that is directly related to the type and amount of solids in solution.

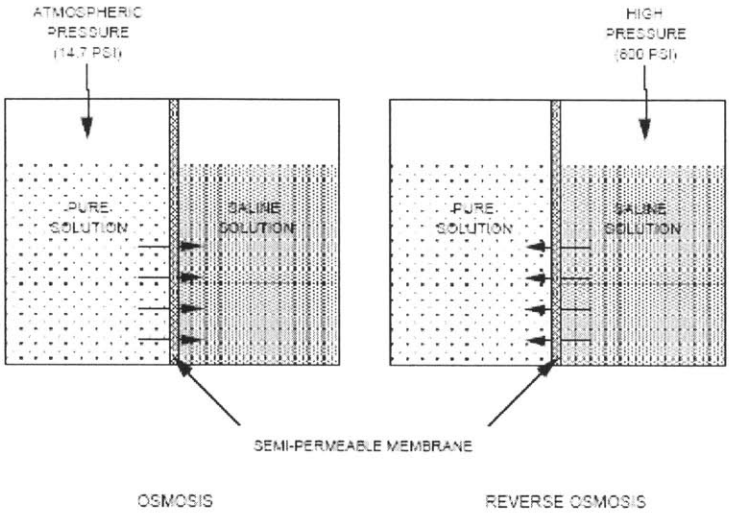

Figure 6-1: Principle of Reverse Osmosis

In an osmotic system, shown in Figure 6-1, the less concentrated solution will attempt to equalize the concentrations of both solutions by migrating across the semi-permeable membrane. When enough pure solution migrates across the membrane such that the inherent potential difference between the solutions in no longer higher than the osmotic pressure of the membrane, the purer solution will stop flowing. If the pressure on the concentrated solution is increased to above the osmotic pressure, fluid flow will be reversed. This condition, called Reverse Osmosis, can be established by artificially pressurizing the more concentrated solution using a high pressure pump.

6.3 Application of Reverse Osmosis

The fundamental goal in any desalination process is a significant reduction in the amount of dissolved solids in water. In a Reverse Osmosis desalination system, most of the dissolved solids do not pass through the membrane but are instead carried along the membrane surface. This rejected water, referred to as brine, becomes increasingly more concentrated as it flows across the surface of the membranes and is eventually piped to drain. A simplified diagram of a Reverse Osmosis system appears as Figure 6-2.

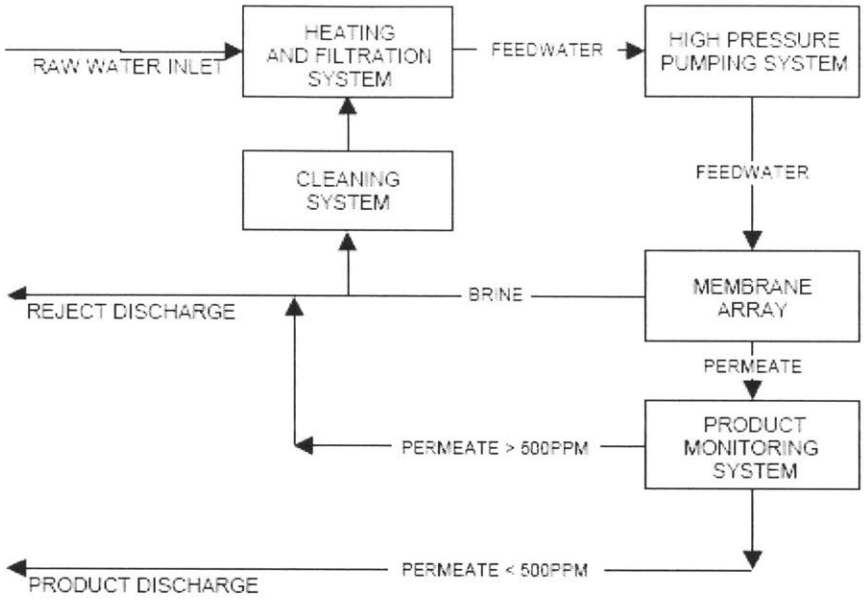

Figure 6-2: Simplified Schematic of an RO System

6.4 *SENECA* Reverse Osmosis System Overview

This Reverse Osmosis system on *SENECA* consists of a 5-micron filter housing, a raw water pump, a high pressure pump, a cleaning valve and a high pressure bypass valve. The clean and filtered raw water (referred to as feed water) flows to the inlet of the high pressure pump. This pump raises feed water pressure to approximately 900 psi, the nominal pressure for optimal system recovery. The pressurized feed water then flows directly into the membrane array. The membrane array is a fixed arrangement of two fiberglass pressure vessels that each contain two Model SW6040 RO membrane elements that are 6" in diameter and 40" in length [26]. The pressurized feed water flows along the membrane surface where reverse osmosis occurs. The feed water flow is divided into two streams; the high purity product stream (referred to as permeate) and the concentrated reject stream (referred to as the brine). After exiting the membrane array, the brine (which contains large concentrations of minerals, salts and other impurities) flows through the High-Pressure Regulation Assembly, through the Reject Flow Meter and then to overboard discharge piping. A check valve is installed on the brine discharge piping to prevent back flow into the system. Figure 6-3 shows a diagram of *SENECA's* reverse osmosis plant.

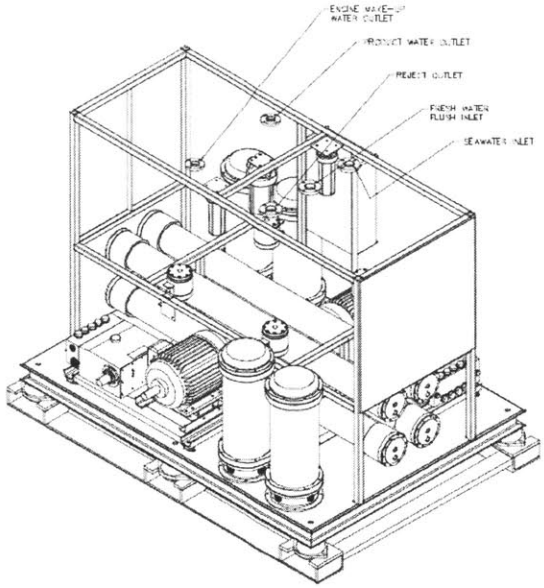

Figure 6-3: *SENECA* Reverse Osmosis Plant

The system is also equipped with a fresh water flush system designed to flush out all seawater from the system when the system is secured. The presence of stagnant seawater within the system can lead to the growth of bacteria, which can ultimately foul the membrane surface. When the fresh water flush mode is activated, water is brought into the system from the ship's fresh water supply. The RO unit is equipped with an activated carbon filter to eliminate chlorine or bromine content that may be present in stored water.

6.5 System Installation

In order to monitor the Reverse Osmosis system on *SENECA*, a NILM was installed on each of the high pressure pumps. Because both pumps are controlled from one power panel, the installation of the current transducers and voltage measurement leads was trivial. Figure 6-4 shows the Reverse Osmosis control panel on *SENECA*. The current transformers can be seen at the bottom of the control panel.

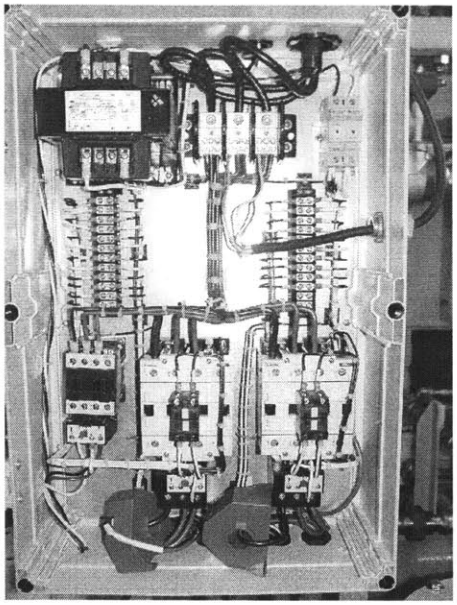

Figure 6-4: Reverse Osmosis Control Panel

6.6 Reverse Osmosis Results

Reverse osmosis data was collected during February of 2005 while the ship was underway on patrol. Due to a high sediment count in the discharge permeate, the "A" pump was secured for the duration of patrol. An example of power data from the "B" appears below in Figure 6-5.

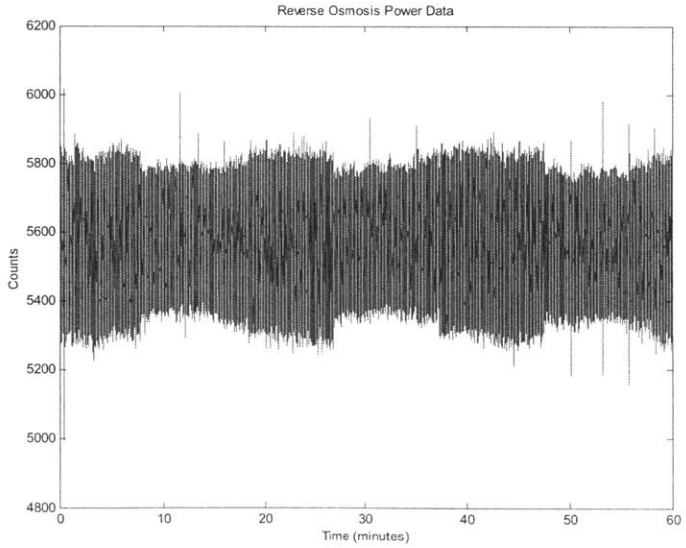

Figure 6-5: Reverse Osmosis NILM Power Data

Figure 6-5 indicates that there is a significant power fluctuation around 5600 counts. A higher resolution of the oscillation is presented in Figure 6-6.

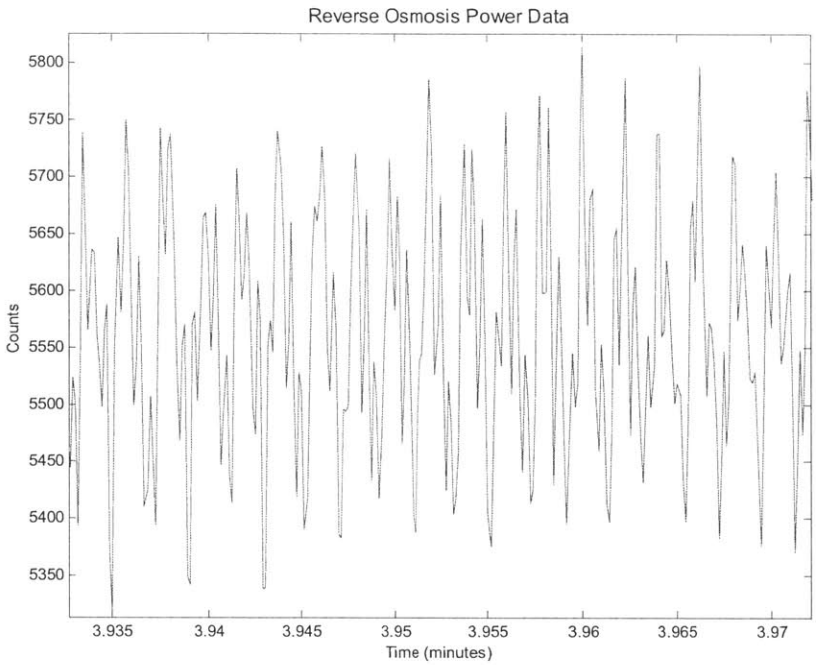

Figure 6-6: Reverse Osmosis Power Data Zoom

The fluctuations observed in Figures 6-5 and 6-6 indicate that the pump power is varying as it runs. A FFT of the power data, shown in Figure 6-7, reveals interesting peaks in the power spectrum at 8 Hz, 16 Hz, 29 Hz and 37 Hz.

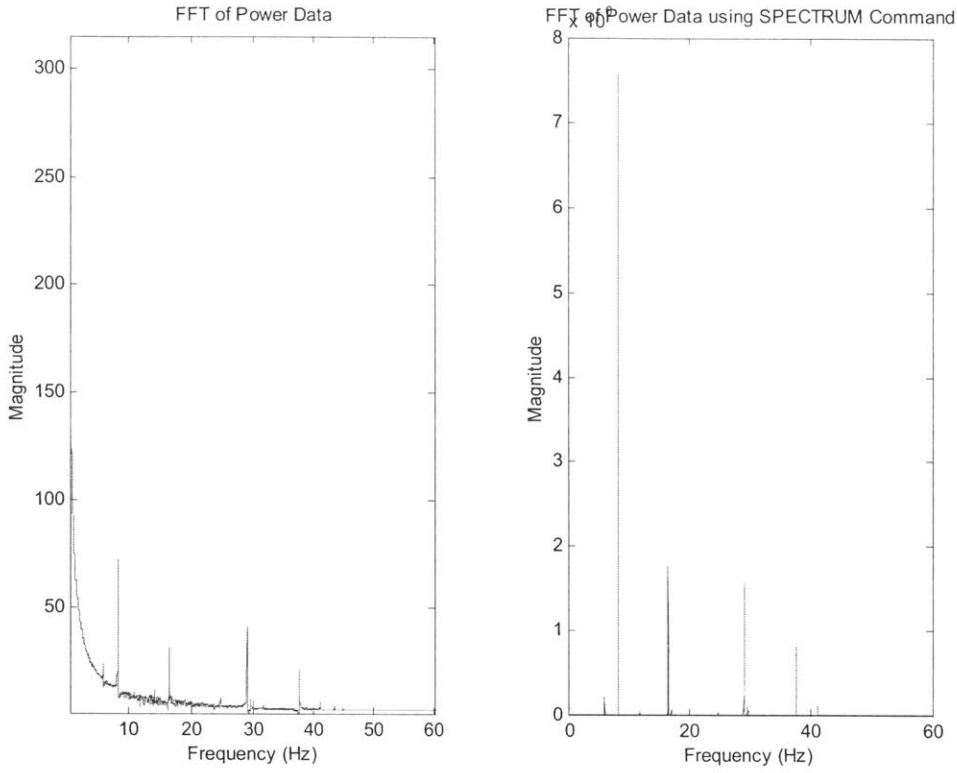

Figure 6-7: Power Spectrum of Reverse Osmosis Pump

The peaks observed in Figure 6-7 appear to be characteristic of the reverse osmosis system. These peaks could also be generated by resonant effects anywhere in the system. They might also be an indication of equipment health and should be monitored in the future. Additional applications of this data are addressed in Chapter 7.3.1.

Chapter 7 Conclusions and Recommendations

7.1 NILM Systems

7.1.1 Application

The full functionality of the NILM should be tested on an operational shipboard engineering plant. One of the most promising features of the NILM is its ability to measure multiple loads simultaneously using only one set of voltage leads and one current transducer [11]. In the current arrangement, each system onboard *SENECA* has its own dedicated NILM. It is recommended that a single NILM be installed at a major shipboard power panel whereby it can continuously monitor the electrical feeds to numerous piece of equipment. Two candidate pieces of equipment for this experiment would be *SENECA's* sewage vacuum and ASW pumps. Although laboratory experiments have demonstrated the ability of the NILM to distinguish between different loads captured from the same source, the shipboard environment may offer additional challenges such as noise and the ability to supply electrical equipment from numerous sources.

7.1.2 System Hardware and Software

A transition from the analog-to-digital conversion card used in the PC to the universal serial bus (USB) interface developed at MIT by fellow students should begin immediately. In addition to being more cost-effective and robust, the USB NILM promises a much higher data collection rate than the current SCSI system. A universal system for storing and backing-up NILM data should also be investigated.

An updated software package which includes trending analysis, automatic data acquisition and storage, load on/off recognition, and recognition of large changes in steady state power level should be installed on all NILM computers. In addition, the specific diagnostic indicators presented in this thesis and the capability to provide fault notification should also be

featured. It is recommended that this software package be installed on *SENECA* immediately, where crew and contractor interest in this system continues to grow.

Another software feature that would be useful would be the ability to automatically remove (delete) empty snapshots. This would especially apply to the reverse osmosis system where during normal system operation only one pump is used (although both pumps are continuously monitored). The option to automatically delete data from the off-line pump would make the analysis and the quantity of data files much more manageable.

7.2 Cross-System Validation

The diagnostic indicators presented in this thesis should be validated on additional engineering systems and/or on different platforms. The leak indicator diagnostic should be applied to additional cycling systems such as the Low Pressure Air Compressor (LPAC) system at the Navy Land Based Engineering System in Philadelphia, PA. Experiments should be conducted to determine if the presence of a leak has a similar impact on the frequency and number of "charging" pump runs. It would also be interesting to categorize the system behavior in terms of the underlying process or statistical distribution. In the case of *SENECA's* sewage system, a Poisson process was observed. Preliminary observations from the LPAC system seem to indicate that this system has a normal distribution with an abnormally small variance [11]. A comparison between these two different types of processes and how they manifest their respective leak rates may also be interesting.

For the coupling failure diagnostic, further experiments should be conducted to determine if the location of the peak observed in the frequency spectrum is a function of the resonant frequency of the system, the coupling parameters or a combination of the two. Experiments on other coupled systems should be performed to ensure similar results are achieved.

7.3 Future Systems

7.3.1 Reverse Osmosis

The reverse osmosis system shows a promising future for NILM based observations. The ability to identify system health, membrane life and amount of dissolved solids seems promising through an analysis of the high pressure pumps. Based on results from the fluid system in Chapter 5, it would appear that the high pressure pumps would show higher power consumption when either the concentration of dissolved solids increased or the membrane permeability decreased. Early identification of membrane failure would minimize the operational impact of an impaired water producing system.

7.3.2 Constant Tension Winch Systems

The Constant Tension Winch System is another system that may be rich in NILM applications. The winches are primarily used to lower *SENECA 's* small boats from the main deck of the cutter to the edge of the water. The ability of the winches to maintain constant tension on the lines increases boat crew safety by helping to reduce the roll and pitch of the small boat when it enters the water. It might even be possible to use the winch power data to determine the local wave action or a generalized sea state. The ability of the NILM to determine payout/retrieval speeds and static/dynamic loading from power would be particularly helpful to the ship and may have additional applications outside of the shipboard environment.

7.4 Conclusions

The NILM has shown promising results in diagnosing pathological equipment failures. The data presented in the preceding chapters illustrate the ability of the NILM to effectively monitor, identify and diagnose problems with electro-mechanical systems on ships. The NILM is also capable of providing backup indications of system performance, trending equipment performance, and recognizing different fault conditions.

By monitoring power consumption, the NILM examines the heartbeat of the electrical system; but the heartbeat is used to determine much more than just the condition of the heart. It has been shown that power consumption can also provide excellent indications concerning the overall health of the system, giving hope and promise to the idea that a highly capable NILM-based automated monitoring system will be a reality in the near future.

List of References

[1] S.B. Leeb, S. R. Shaw, and J. L. Kirtley, Jr. 1995. "Transient Event Detection in Spectral Envelope Estimates for Non-instrusive Load Monitoring," *IEEE Transactions on Power Delivery* Vol. 10 No. 3, pp. 1200-1210.

[2] Norford, L. K. and S. B. Leeb. 1996. "Non-intrusive Electrical Load Monitoring." *Energy and Buildings*, Vol. 24, pp. 51-64.

[3] S.B. Leeb. "A Conjoint Pattern Recognition Approach to Non-intrusive Load Monitoring," Ph.D. Dissertation, Department of Electrical Engineering and Computer Science, Massachusetts Institute of Technology, Cambridge, MA, 1993.

[4] K.D. Lee, S.B. Leeb, L.K. Norford, P. Armstrong, J. Holloway and S.R. Shaw, Estimation of Variable Speed Drive Power Consumption from Harmonic Content, accepted for publication, *IEEE Transactions on Energy Conversion.*

[5] Shaw, S.R., D. Evangelista, S.B. Leeb, and C.R. Laughman, Non-intrusive Load Monitoring and Identification in an Automotive Environment, *Proceedings of ELECTRIMACS 1999*, Lisbon, Portugal, pp. 199-204, September 1999.

[6] Timothy J. McCoy, private communication, February 2005.

[7] H. Bruce Land III, "Sensing Shipboard Arc Faults", *IEEE Power Engineering Review,* Vol. 22, Issue 4, pp. 18-20, 27, April, 2002.

[8] M. DiUlio, C. Savage, B. Finley, and E. Schneider, "Taking the Integrated Condition Assessment System to the Year 2010," *Thirteenth International Ship Control Systems Symposium,* Orlando, Florida, April 7-9, 2003.

[9] J. Steven Ramsey, "Shipboard Applications of Non-Intrusive Load Monitoring", MIT NSEE/S.M. EECS thesis, June 2004.

[10] Shaw, S.R., "System Identification Techniques and Modeling for Non-intrusive Load Diagnostics," Ph.D. Dissertation, Department of Electrical Engineering and Computer Science, Massachusetts Institute of Technology, Cambridge, MA, February, 2000.

[11] Greene, William, "Evaluation of Non-Intrusive Monitoring for Condition Based Maintenance Applications on U.S. Navy Propulsion Plants," MIT, S.M. NAME/ S.M. ME thesis, June 2005.

[12] S.R. Shaw, S.B. Leeb, Identification of Induction Motor Parameters from Transient Stator Current Measurements, *IEEE Transactions on Industrial Electronics*, Volume 46, No. 1, February 1999, pp. 139-149.

[13] B.S. Payne, S.M. Husband, and A. D. Ball, "Development of Condition Monitoring Techniques for a Transverse Flux Motor", *International Conference on Power Electronics, Machines and Drives,* pp. 139-144, June, 2002.

[14] P. Armstrong, "Model Identification with Application to Building Control and Fault Detection", Building Technology, Massachusetts Institute of Technology, Cambridge, MA, 1993.

[15] Kwangduk Douglas Lee, *Electric Load Information system based on Non-Intrusive Power Monitoring,* pp. 23-27, Massachusetts Institute of Technology, June, 2003.

[16] LT Mike Obar, USCG, personal communication, August 13, 2004.

[17] Zwillinger, *CRC Standard Mathematical Tables and Formula,* CRC Press, New York, NY, 1996, pp. 595.

[18] Dimitri P. Bertsekas, and John N. Tsitsiklis, *Introduction to Probability*, Athena Scientific, Belmont, MA, 2002, pp. 293.

[19] "Sure-Flex Elastometic Couplings," TB Wood's Incorporated, Chambersburg, PA, 17201.

[20] Adel A. Shaltout, "Analysis of Torsional Torques in Starting of Large Squirrel Cage Induction Motors," Jordan University of Science and Technology, Irbid, Jordan.

[21] Steven B. Leeb, MATLAB Scripts indaparam.m, ind.m, convind.m and class notes, *6.11s: Design of Motors, Generators and Drive Systems,* Massachusetts Institute of Technology, 2003.

[22] Paul C. Krause, Oleg Wasynczuk, Scott Sudhoff, Analysis of Electric Machinery, West Layfette, IN, pp. 410, 1986.

[23] LT Mike Obar, USCG, personal communication, March 28, 2005.

[24] K.D. Lee, S.B. Leeb, L.K. Norford, P. Armstrong, J. Holloway and S.R. Shaw, Estimation of Variable Speed Drive Power Consumption from Harmonic Content, accepted for publication, *IEEE Transactions on Energy Conversion.*

[25] SETRA Model 230 Installation Guide, SETRA Systems Inc., Boxborough, MA, Jan 2001.

[26] Village Marine Tec., "Operation Manual for USCG Model RC7000 Plus Reverse Osmosis Desalination Plant," Gardena, CA 2005.

Appendix A: Sewage Simulation MATLAB Code

This appendix contains scripts used to simulate operation of *SENECA's* sewage system. The first script calculates the expected time until the next flush. The second script simulates the system behavior while waiting for the next flush of the system. The scripts were written by the author and James Paris, a fellow student at MIT's Laboratory for Electromagnetic and Electronic Systems (LEES).

A.1 SEWAGE_SIMULATION.M

```
% Parameters
global pump1_rate pump2_rate pump_low pump_lower pump_high leak;
T = 24*7;                   % simulation time (hours)
flush_drop = 1;             % pressure drop of single flush
pump1_rate = 19 * 60;       % rate for first pump, hg/hour
pump2_rate = 17 * 60;       % rate for second pump, hg/hour
pump_low = 14;              % one pump turns on
pump_lower = 12;            % both pumps turn on
pump_high = 18;             % both pumps turn off
leak = 20;                  % leak rate, hg/hour
lambda = 40;                % average flushes per hour

clf;
colordef('white');
pressure = pump_high;
pump_time = [];

% Simulate flushes for the entire time period
t = 0;
lastt = 0;
while (t < T),
  % Run the pumping/leaking simulation to get us caught up
  [ pressure, tmptime ] = pumpleak(pressure, t - lastt);
  pump_time = [ pump_time, tmptime + lastt ];

  % Now we're caught up with pumping, so flush the toilet.
  pressure = pressure - flush_drop;

  % Jump forward to next flush
  lastt = t;
  t = t - log(rand) / lambda;
end
```

```
[N, X] = hist(diff(pump_time),100);
figure(1);
whitebg(1,'white');
plot(X*60,N,'b');
xlabel('Time Between Pump Runs (min)','fontsize',18);
ylabel ('Counts','fontsize',18);
%pause(0.25);
%end

for i=1:length(N)
  if N(i)==max(N)
     count=i;
  end
end
```

A.2 PUMPLEAK.M

```
function [ pressure, turnons ] = pumpleak(pressure, T)
 % Simulate the pumping / leaking for 't' hours
 global pump1_rate pump2_rate pump_low pump_lower pump_high leak;

 persistent pumps_running;
 if (T == 0)
   pumps_running = 0;
 end

 if (pressure < 0)
   error('Pressure is negative!  Too much flushing?\n');
 end

 t = 0;
 turnons = [];
 while(t < T),
   left = T - t;

   % Figure out the current pressure rate
   if (pressure <= pump_lower | pumps_running == 2)
     rate = pump1_rate + pump2_rate - leak;
     if(pumps_running ~= 2)
          turnons = [ turnons, t ];
          pumps_running = 2;
     end
   elseif (pressure <= pump_low | pumps_running == 1)
```

```
  rate = pump1_rate - leak;
  if(pumps_running ~= 1)
      turnons = [ turnons, t ];
      pumps_running = 1;
  end
 else
  rate = -leak;
  pumps_running = 0;
 end

 % Now jump forward until we run out of time or something may change
 if (rate == 0)
  t = T;
 else
  if (pumps_running == 2 & rate < 0)
      error('Both pumps running and still losing pressure due to leak!');
  elseif (pumps_running == 1 & rate < 0)
      % Run until we need two
      stop = pump_lower;
  elseif (rate < 0)
      % Run until we need one
      stop = pump_low;
  elseif (rate > 0)
      % Run until we need none
      stop = pump_high;
  end

  turnoff = (stop - pressure) / rate;
  if (t + turnoff < T)
      t = t + turnoff;
      pressure = stop;
      pumps_running = 0;
  else
      t = T;
      pressure = pressure + rate * left;
  end
 end
end
```

Appendix B: Induction Motor Simulation

This appendix contains scripts used to simulate operation of a centrifugal pump. The first script combines all subroutines of the motor simulation script and allows us to create an FFT of the motor power. The second script solves the state equations and produces a plot of the real power consumed by the electric motor vs. time. The remaining 3 scripts are used to calculate the currents, voltages and torque used by the motor. The scripts indparam-noload.m, convind_noload.m and ind_noload.m were written by Steven B. Leeb as part of [21]. The scripts C.1 – C.5 below simulate the operation of a centrifugal pump at no load. For the loaded case, additional mechanical state equations must be added to the simulation. An example of this code appears as C.6.

B.1 MOTORSIM.M

```
% This script runs the motor simulation and retrieves lab frame quantities.

clear;
runind_noload;
[m,m2]=convind_noload(tout,y);
ids = m(:,1);
iqs = m(:,2);
idr = m(:,3);
iqr = m(:,4);

T = m2(:,1);
ias = m2(:,2);
ibs = m2(:,3);
ics = m2(:,4);
vas = m2(:,5);
vbs = m2(:,6);
vcs = m2(:,7);

% As a check, plot the torque.

figure(1);
hold off;
clf;
plot(tout,T);
hold on;
grid on;
title('Torque v. Time - No Load');
ylabel('Torque: N-m');
```

```
xlabel('Time: Sec');
hold off;

P=ias.*vas+ibs.*vbs+ics.*vcs;
P_spect=fft(P(1:1800).*hanning(1800),4096);
f=[0:8000/4096:4095*(8000/4096)];
figure(4)
plot(f,abs(P_spect),'k');
```

B.2 RUNIND_NOLOAD.M

```
% This script runs the AC induction motor simulation during free acceleration

% This software is distributed in the hope that it will be useful, but WITHOUT ANY
% WARRANTY.  It is for educational use only.  Please do not distribute or sell this software, or
% remove the copyright notice.
%
%  Copyright, 1995, 1998, 2000  Steven B. Leeb

clear;
indparam_noload

% In order to run data through prep, we should have data with approximately 128 samples per
% period and a few hundred cycles.  We'll create a time vector with a sampling frequency of
% 8kHz, which is what the PCI-170 card is set for, and we'll generate data over 5 seconds.

total_t = 5;  % Create 5 seconds worth of data
T = (1/8000); % Sampling frequency is 8kHz
t = (0:T:total_t);
time = t';
%time = [0 .5]';
state0 = [0 0 0 0 0 0]';
[tout,y] = ode45('ind_noload',time, state0);
%plot(tout,y(:,5));
%xlabel('Time, Seconds');
%ylabel('Electrical Rotor Speed, Rads per Second')
%title('Motor Spin-up');
```

B.3 INDPARAM_NOLOAD.M

```
% This script loads the machine parameters for a 3hp, 180 V (L-N, peak) AC induction machine
% into the global environment.
% This software is distributed in the hope that it will be useful, but WITHOUT ANY
% WARRANTY.  It is for educational use only.  Please do not distribute or sell this software, or
% remove the copyright notice.
```

```
%
%  Copyright, 1995, 1997, 1998, 2000  Steven B. Leeb

global P rs rr Xm X1s X1r we J Bl vds vqs vqr vdr Tl

% These are the machine parameters for a 50 Hp, 230V (L-L, peak) AC induction machine.

P = 4;          % Number of poles (*not* pole pairs)
rs = 0.435;     % Stator resistance
rr = 0.816;     % Rotor resistance
Xm = 26.13;  % Magnetizing Impedance, in Ohms on a 60 Hz base
X1s = 0.754;  % Stator Side Leakage Impedance, in Ohms on a 60 Hz base
X1r = 0.754;  % Rotor Side Leakage Impedance, in Ohms on a 60 Hz base
we = 377.;      % Base electrical frequency, rads per second (60 Hz)
J = .089;       % Rotor Inertia
Bl = 0;         % Load Damping Coefficient
vds = 0.0;      % D axis stator voltage
vqs = 180.0;  % Q axis stator voltage
vqr = 0.0;      % D axis rotor voltage
vdr = 0.0;      % Q axis rotor voltage
Tl = 0.0;       % Load torque
```

B.4 CONVIND_NOLOAD.M

```
function [m,m2] = convind_noload(t,y);
%  [m,m2] = convind(t,statev)
%
% This script transforms the DQ stator and rotor fluxes computed using ind.m and ode45 back
% into laboratory frame stator currents and voltages, e.g., ias and vas for phase a.
%
% The variable w determines the reference frame in which the simulation will be conducted.
% With w = 377, the simulation variables will be in a synchronously rotating reference frame.
%
% On return, the output matrices m and m2 contain:
%       m = [ids iqs idr iqr];
%       m2 = [T ias ibs ics vas vbs vcs];
% This script also plots the simulated rotor torque versus speed on return.
%
%  This software is distributed in the hope that it will be useful, but WITHOUT ANY
% WARRANTY.  It is for educational use only.  Please do not distribute or sell this software, or
% remove the copyright notice.
%
%  Copyright, 1995, 1998, 2002  Steven B. Leeb

global P rs rr Xm X1s X1r we J Bl vds vqs vqr vdr Tl
```

```
w = 377.;

Lm  = Xm/we;  % This is the magnetizing inductance
L1s = X1s/we; % Stator leakage
L1r = X1r/we; % Rotor leakage
Las = L1s + Lm;
Lar = L1r + Lm;

lamqs = y(:,1);
lamds = y(:,2);
lamqr = y(:,3);
lamdr = y(:,4);
wr    = y(:,5);
th    = y(:,6);

D = Lm*Lm - Las*Lar;
idr  = (Lm*lamds - Las*lamdr)/D;
iqr  = (Lm*lamqs - Las*lamqr)/D;
iqs  = (Lm*lamqr - Lar*lamqs)/D;
ids  = (Lm*lamdr - Lar*lamds)/D;
```

B.5 IND_NOLOAD.M

```
function [slopes] = ind_noload(t,statev)
%  [slopes] = ind(t,statev)
%
% This script computes the state variable derivatives for a fifth order model of a balanced, three
% phase AC induction machine. The state variables are the D and Q stator and rotor fluxes, and
% the rotor speed (wr).Use this script with ODE45 to simulate the performance of the induction
% machine.
%
% Run indparam.m to load sample machine parameters before simulating.
%
% This software is distributed in the hope that it will be useful, but  WITHOUT ANY
% WARRANTY.  It is for educational use only.  Please do not  distribute or sell this software, or
% remove the copyright notice.

%  Copyright, 1995, 1998, 2002  Steven B. Leeb

% The variable w determines the reference frame in which the simulation will be conducted.
% With w = 377, the simulation variables will be in a synchronously rotating reference frame.

global P rs rr Xm X1s X1r we J Bl vds vqs vqr vdr Tl
w = 377.;
Lm  = Xm/we;  % This is the magnetizing inductance
L1s = X1s/we; % Stator leakage
```

```
L1r = X1r/we; % Rotor leakage
Las = L1s + Lm;
Lar = L1r + Lm;

lamqs = statev(1);
lamds = statev(2);
lamqr = statev(3);
lamdr = statev(4);
wr    = statev(5);
th    = statev(6);

D = Lm*Lm - Las*Lar;
idr   = (Lm*lamds - Las*lamdr)/D;
iqr   = (Lm*lamqs - Las*lamqr)/D;
iqs   = (Lm*lamqr - Lar*lamqs)/D;
ids   = (Lm*lamdr - Lar*lamds)/D;

s1 = (vqs - w*lamds - rs*iqs);
s2 = (vds + w*lamqs - rs*ids);
s3 = (vqr - (w - wr)*lamdr - rr*iqr);
s4 = (vdr + (w - wr)*lamqr - rr*idr);
% P is the number of poles, *not* pole pairs
T  = (3/2)*(P/2)*(lamqr*idr - lamdr*iqr);
s5 = (P/2)*(T - Tl)/J;
s6 = 377;
slopes = [s1 s2 s3 s4 s5 s6]';
```

B.6 IND_LOAD.M

```
function [slopes] = ind_test2(t,statev)
%  [slopes] = ind(t,statev)
%
% This script computes the state variable derivatives for a fifth order model of a balanced, three
% phase AC induction machine. The state variables are the D and Q stator and rotor fluxes, and
% the rotor speed (wr).Use this script with ODE45 to simulate the performance of the induction
% machine.
%
% Run indparam.m to load sample machine parameters before simulating.
%
% This software is distributed in the hope that it will be useful, but WITHOUT ANY
% WARRANTY.  It is for educational use only.  Please do not distribute or sell this software, or
% remove the copyright notice.

%  Copyright, 1995, 1998, 2002  Steven B. Leeb

% The variable w determines the reference frame in which the simulation will be conducted.
```

```
% With w = 377, the simulation variables will be in a synchronously rotating reference frame.
%
%  MODIFIED: wr is now rotor mechanical speed and not electrical rotation speed.

global P rs rr Xm X1s X1r we Jm Jp Bl vds vqs vqr vdr Cc K Tload
w = 377.;
Lm  = Xm/we;  % This is the magnetizing inductance
L1s = X1s/we; % Stator leakage
L1r = X1r/we; % Rotor leakage
Las = L1s + Lm;
Lar = L1r + Lm;

lamqs = statev(1);
lamds = statev(2);
lamqr = statev(3);
lamdr = statev(4);
wr    = statev(5);
thr   = statev(6);
wp    = statev(7);
thp   = statev(8);
th    = statev(9);


D = Lm*Lm - Las*Lar;
idr  = (Lm*lamds - Las*lamdr)/D;
iqr  = (Lm*lamqs - Las*lamqr)/D;
iqs  = (Lm*lamqr - Lar*lamqs)/D;
ids  = (Lm*lamdr - Lar*lamds)/D;

s1 = (vqs - w*lamds - rs*iqs);
s2 = (vds + w*lamqs - rs*ids);
s3 = (vqr - (w - (P/2)*wr)*lamdr - rr*iqr);
s4 = (vdr + (w - (P/2)*wr)*lamqr - rr*idr);
% P is the number of poles, *not* pole pairs
Te  = (3/2)*(P/2)*(lamqr*idr - lamdr*iqr);  % Electrical torque
s5 = (1/Jm)*(Te - Cc*(wr-wp)-K*(thr-thp)); % Equation for rotor mechanical speed
s6 = wr;
s7 = (1/Jp)*(Cc*(wr - wp) + K*(thr-thp)-Tload);
s8 = wp;
s9 = 377;
slopes = [s1 s2 s3 s4 s5 s6 s7 s8 s9]';
```